ORIGINAL PAPER

A numerical framework for modelling tire mechanics accounting for composite materials, large strains and frictional contact

A. Cornejo[1,2] · V. Mataix[1] · P. Wriggers[3] · L. G. Barbu[1,2] · E. Oñate[1,2]

Abstract

We present a general framework for the analysis and modelling of frictional contact involving composite materials. The study has focused on composite materials formed by a matrix of rubber and synthetic or metallic fibres, which is the case of standard tires. We detail the numerical treatment of incompressibility at large deformations that rubber can experience, as well as the stiffening effect that properly oriented fibres will induce within the rubber. To solve the frictional contact between solids, a Dual Augmented Lagrangian Multiplier Method is used together with the Mortar method. This ensures a variationally consistent estimation of the contact forces. A modified Serial-Parallel Rule of Mixtures is employed to model the behaviour of composite materials. This is a simple and novel methodology that allows the blending of constitutive behaviours as diverse as rubber (very low stiffness and incompressible behaviour) and steel (high stiffness and compressible behaviour) taking into account the orientation of the fibres within the material. The locking due to the incompressibility constraint in the rubber material has been overcome by using Total Lagrangian mixed displacement-pressure elements. A collection of numerical examples is provided to show the accuracy and consistency of the methodology presented when solving frictional contact, incompressibility and composite materials under finite strains.

1 Introduction

The importance of pneumatic tires for vehicles like automobiles, trucks, bicycles and buses has continuously increased since its commercial introduction in Europe in the 1950's [1]. Among other characteristics, the success of this technology is due to its high endurance, good wear and handling, low weight and a reduced energy consumption.

The development and manufacturing of classical tire structures and new environmentally friendly constructions fulfilling the current high operating standards imply the

✉ A. Cornejo
acornejo@cimne.upc.edu

1   Centre Internacional de Mètodes Numèrics en Enginyeria (CIMNE), Campus Norte UPC, 08034 Barcelona, Spain

2   Universidad Politécnica de Cataluña (UPC), Campus Norte UPC, 08034 Barcelona, Spain

3   Institute of Continuum Mechanics, Leibniz University of Hannover, Appelstr. 11, 30167 Hannover, Germany

conception and conduction of an exhaustive series of experimental studies to asses the performance and safety of the proposed designs [2, 3], which is expensive in both time and monetary terms. In this regard, numerical methods like the Finite Element Method (FEM) can contribute to the reduction of this experimental cost, enabling the estimation of the stress/strain states of the tire under a wide range of loading conditions. With the FEM, and after a proper material characterisation, a very precise and detailed analysis of a design can be performed and corrected before production starts [2, 4–6]. Conversely, structures formed by cord-reinforced rubber materials, which is the case of study in this work, are characterised by a high complexity in the numerical analysis. In the case of tires, they are formed by several layers of parallel fibres (cords) made of different materials as nylon, polyester and steel. These fibres can have different spatial orientations and volumetric participation and are embedded in a rubber type matrix. One can easily infer from the previous description that a tire is a complex structure to model, especially taking into account the geometrical and constitutive non-linearities that can arise from its analysis [7–9].

Generally, the tire is conformed by several layers of interconnected parts with different material properties, i.e. sidewall, tread, bead core, etc. The development of a numerical tool that can accurately reproduce the mechanical behaviour of this kind of complex composite structures in an efficient way is of paramount importance and, due to its major complexity, it has not been fully resolved in literature.

Historically, an approach to model this kind of composite material was using laminated shell elements combining isotropic (rubber) and orthotropic behaviours (cords) [10]. Later, by adapting the composite theories applied to laminates, the material properties of each individual constituent were averaged over a Finite Element (FE) by an orthotropic or anisotropic constitutive law, always restrained to small displacements and strains [11, 12] and mostly within elasticity. Another option consists in defining a set of rebar elements, which represent the effect of several cord layers in combination with standard rubber FE [6]. Line cord elements can either link two already existing rubber nodes, which complicates the mesh generation in order to properly orient the fibres in the solid, or an intersection procedure has to be performed in order to estimate the deformational state of the fibres within the rubber. As expected, the previous approach requires a detailed geometrical description of the model in terms of the positioning and orientation of each cord, which can substantially increase the preprocessing time. The strong point of this methodology is that it allows the use of different constitutive models for each material constituent, even though the one applicable to the cord must be one-directional. More recently, approaches like the one proposed in Wriggers et al. [13] use the Virtual Element Method (VEM) [14] solving the incompressibility constraint and it is generalised to include the effect of inextensive fibres. Even though the results are good, the implementation of the VEM is not trivial and, for the case of inextensive fibres, a new set of Lagrange Multipliers (LM) related to the fibre stresses has to be accounted for via the Finite Element Analysis (FEA), which increases the complexity of the numerical approach.

In this work, an adapted version of the existing Serial-Parallel Rule of Mixtures (SP-RoM) [15–18] is proposed. The methodology can be seen as a phenomenological homogenisation of the material constituents, splitting their behaviour in the so-called parallel (aligned to the fibre) and serial (the remaining directions). The SP-RoM allows the use of any constitutive model used under small and large strains. Some modifications of the SP-RoM are detailed to simulate finite strains processes and incompressibility constraints. Special operations have been developed to combine constituent materials with very different stiffnesses, which is the case of mixing rubber and steel cords. By using this methodology, the meshing and preprocessing efforts are minimal, since the amount and orientation of the cords are assigned at the constitutive level, with total modularity and generality

regarding the material laws behaviours. In the case of several layers with different volumetric participation of fibres and/or orientations, a nested stacking of layers can be used within one single element, avoiding to discretize each layer with the FEM, reducing notably the number of degrees of freedom without losing accuracy. The proposed methodology can be easily integrated in the global workflow of a FEM code without the need of major implementations, other than making use of a mixed $u - p$ formulation and the adequate SP-RoM constitutive law.

One of the main goals of tires is to ensure a sufficient adherence to the ground when the vehicle is turning, accelerating or breaking, among other situations. This means that the frictional contact between the tire and the ground surface is a relevant and decision-making issue when designing the geometry and material of the tire. Due to the relevance in the field of study, a frictional computational contact mechanics methodology for solids has been implemented and benchmarked via a wide range of standard problems involving the contact of fibre-reinforced rubber materials. In this regard, a state of the art Dual Augmented Lagrange Multipliers Method (DALMM) in combination with the Mortar Method has been implemented [19–21], enabling a fully consistent gap estimation and an exact contact constraint enforcement. All the developments have been implemented within the open-source FE code Kratos-Multiphysics environment [22, 23] and are fully available.

1.1 Pneumatic tire mechanics

A tire is a very complex composite structure, embedded in a highly flexible and nearly-incompressible material (rubber), several layers of stiff parallel string reinforcements made of fabric and/or steel are placed in different proportions and orientations [4, 24, 25]. Figure 1 shows a schematical view of the different materials and layers that a general tire can present. In the same figure one can see how the more superficial reinforcement is usually aligned with the generatrix of the tire (in blue). Then several layers of properly oriented layers are placed (red and green). A layer parallel to the sidewall includes a radial reinforcement to increase the vertical stiffness of the tire. Finally, a steel loop (bead) is placed close to the rim contact to hold the tire to the wheel.

In mechanical terms, the rubber can be seen as a flexible matrix that holds the fibre reinforcement in place and a material that offers a good frictional performance when contacting against the ground. The material properties of the rubber can be different depending on their functionality: the tread (grey area in Fig. 1) has to be much harder that the rubber used in the sidewall. Conversely, the fibres used (steel or fabric) offer a high stiffness contribution in tension (in compression they can buckle) and provide tire rigidity and puncture resistance. In this regard, the material, positioning, quantity and
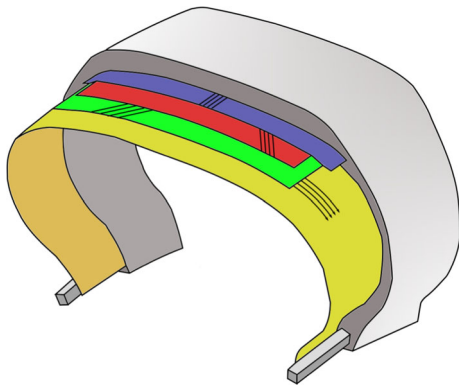
Fig. 1 Schematic model section representing different regions of a tire. Black strips indicate the different orientations that the cords and steel fibres can present

orientation of the reinforcement are the most relevant factors related to the performance of a tire.

In modelling terms, a tire is a flexible structure under arbitrary loads, displacements, rotations, impacts, etc. This implies that a numerical tool must be capable of capturing accurately finite strains of the material and large displacements. As detailed in Sect. 2, a Total Lagranian (TL) description of motion has been used to capture the kinematics of the problem at hand. The quasi-incompressibility exhibited by the rubber can induce a "locking" of the solution when using standard displacement-based FEM. A mixed displacement-pressure ($u - p$) formulation has been implemented to overcome this numerical issue. In order to model the fibre contribution to the global behaviour of the composite material, a modified version of the SP-RoM methodology for finite strains has been used, which efficiently reproduces the behaviour of long-fibre reinforced composites. Finally, in order to properly simulate the different orientations that the fibre layers can present, a rotation of the local axes of the FE (cylindrical coordinates) and a posterior rotation of the local axes of each layer within the FEM have been implemented.

Summarising, this work presents an implicit numerical framework for studying in an efficient and accurate way tire mechanics, including the following requirements:

- A non-linear complex composite material, taking into account the quasi-incompressibility and high flexibility of the rubber, as well as the orientation and position of the steel/fibre cords which its stiffness can be 10,000 times higher than the rubber.
- Large displacements and finite strains of the material components. This allows the modelization of tires under any loading and boundary conditions.
- The "micro-buckling" effect of the fibres is tackled, as it can be relevant when the composite material is submitted to compressive loads.

- A general constitutive law for the composite material constituents. We have used incompressible Neo-Hookean or Mooney Rivlin hyperelastic laws for the rubber and compressible Neo-Hookean laws for the fibres.
- An automatic orientation of the fibres of each layer.
- Frictional contact between solids. This is of paramount importance for tire mechanics, in order to ensure a sufficient adherence of the tyre to the ground.

2 Constitutive modelling: finite strain composite materials treatment for tires

In this section, a description of the constitutive models used for the material constituents (rubber and fibres) is provided. The methodologies used to combine the material constituents behaviour to obtain the composite mechanical response are described. One important contribution of this work is the generalisation of the SP-RoM to deal with finite strains and to overcome the numerical instabilities that the incompressibility of the rubber and the high stiffness the fibres may induce.

2.1 Constitutive modelling of material constituents

2.1.1 Quasi-incompressible rubber

The near-incompressibility exhibited by many hyperelastic materials like rubber induces a hydrostatic pressure that can be applied to that material without any change in shape and, at the same time, maintaining a certain stress level [26, 27]. This implies that the stress in this kind of materials cannot be uniquely determined only from strains. This incompressibility issue results in an ill-conditioning of the stiffness matrix and "locking" problems in purely displacement-based FEM. Locking means that the constraint conditions due to incompressibility related to the pure volumetric mode, can only be fulfilled with a stiffening of the bending modes [27]. Several approaches can be used to overcome this limitation, the simplest one consists in sub-integrating the volumetric deformation terms by using low-order integration rules [28]. Unfortunately this approach looses accuracy and stability when FE are subjected to large strains. Another alternative consists in using *F-bar* elements [29], based on the use of a compatible deformation gradient field with an assumed counterpart. This approach is quite straightforward but is limited to quadrilaterals/hexahedras and its consistent linearization is rather complex. Finally, the use of multi-field or mixed principles [27] are based on the idea of not only including the displacement field, but also the volumetric strain or pressure fields. In their general form they have the disadvantage of increasing considerably the number of degrees of freedom (DoF) of the system, which is computationally expensive.

However, in some cases, a static condensation at FE level of the pressure DoF can be performed, thereby mitigating this problem. That said, and being one of the simplest and polivalent approaches, a mixed $u - p$ TL element has been selected to deal with incompressibility. The implementation is based on the work of Comellas et al. [26]. where the classical displacement field (**u**) is complemented by the the elemental pressure p, which interpolation is different from the one used for the displacements. In this case, the equations of motion in residual form can be written as:

$$\begin{bmatrix} \mathbf{K}_{uu} & \mathbf{K}_{up} \\ \mathbf{K}_{pu} & K_{pp} \end{bmatrix} \begin{bmatrix} \Delta \mathbf{u} \\ \Delta p \end{bmatrix} = \begin{bmatrix} \mathbf{f}^{ext} \\ 0 \end{bmatrix} - \begin{bmatrix} \mathbf{f}_u^{int} \\ f_p^{int} \end{bmatrix} \qquad (1)$$

where $\mathbf{f}^{ext}$ is the external forces vector whereas the **K** matrices and the internal forces vector $\mathbf{f}^{int}$ can be obtained via [26]

$$\mathbf{K}_{uu} = \int_{\Omega_0} \mathbf{B}^T \, \mathcal{C}_t \, \mathbf{B} \, d\Omega_0 + \int_{\Omega_0} \mathcal{B}^T \, \mathbf{S} \, \mathcal{B} \, d\Omega_0 \qquad (2)$$

$$\mathbf{K}_{up} = -\int_{\Omega_0} \mathcal{B}^T \, J \, \mathbf{C}^{-1} \, d\Omega_0 = \mathbf{K}_{pu}^T \qquad (3)$$

$$K_{pp} = -\int_{\Omega_0} \frac{1}{\kappa} \, d\Omega_0 \qquad (4)$$

$$\mathbf{f}_u^{int} = \int_{\Omega_0} \mathbf{B}^T \, \mathbf{S} \, d\Omega_0 \qquad (5)$$

$$f_p^{int} = \int_{\Omega_0} (J - 1) + \frac{p}{\kappa} \, d\Omega_0 \qquad (6)$$

where **B** and $\mathcal{B}$ are the standard linear and non-linear strain–displacement transformation matrices, respectively, $\mathcal{C}_t$ is the tangent constitutive matrix, Ω_0 is the reference configuration domain, κ is the bulk modulus, **S** is the second Piola-Kirchhoff stress vector, J is the Jacobian determinant of the deformation gradient tensor and p is the pressure obtained.

Since the pressure p is defined only at element level, the equations to be solved in Eq. (1) can be condensed and reduced to:

$$\bar{\mathbf{K}} \Delta \mathbf{u} = \mathbf{f}^{ext} - \bar{\mathbf{f}}^{int}, \qquad (7)$$

where

$$\bar{\mathbf{K}} = \mathbf{K}_{uu} - \mathbf{K}_{up} K_{pp}^{-1} \mathbf{K}_{up}^T \qquad (8)$$

and

$$\bar{\mathbf{f}}^{int} = \mathbf{f}_u^{int} - \mathbf{K}_{up} K_{pp}^{-1} f_p^{int}. \qquad (9)$$
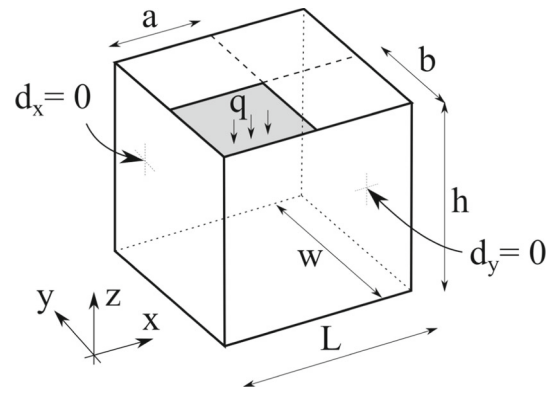
Fig. 2 Nearly-incompressible block submitted to a partial load, original source Schroder et al. [31]

With this $u - p$ FEM methodology the locking effect when modelling nearly-incompressible materials is overcome. Next, it is required to define a proper hyperelastic law for the rubber material which, in order to be consistent with the mixed u-p FE, has to distinguish the volumetric and deviatoric terms. That said, the energy density function of the Neo-Hookean case results in [26]:

$$\Psi = \tilde{\Psi} + \Psi_{vol} = C_1(\tilde{I}_C^{(1)} - 3) + \frac{1}{2}\kappa(J - 1)^2, \qquad (10)$$

where $C_1 = \mu/2$ (Lamé constant) and $\tilde{I}_C^{(1)} = J^{-2/3} I_C^{(1)}$ the *volume-preserving* first invariant of the right Cauchy-Green tensor **C**. Differentitation of the energy density function with respect to **C** yields the constitutive equation in the reference configuration

$$\mathbf{S} = 2C_1 J^{-2/3} (\mathbf{I} - \frac{1}{3} I_C^{(1)} \mathbf{C}^{-1}) - pJ\mathbf{C}^{-1}. \qquad (11)$$

The related tangent tensor is defined in Comellas et al. [26] but in this work the expression has been automatically derived by using the AceGen software [30].

Minimal quasi-incompressible material example A simple example of a quasi-incompressible classical benchmark is solved to demonstrate the stability and accuracy of the element implementation performed in this work. The example consists in an incompressible solid block under a constant partial load. The problem was proposed in Schröder et al. [31] as a benchmark to asses the stability of the FEM when solving incompressible materials and singularities in the Neumann boundary conditions. The geometry of the problem is depicted in Fig. 2. The dimensions in *mm* are: $h = 50$, $w = 50$, $l = 50$, $a = 25$, $b = 25$ and the load $q = 3$ MPa. The upper surface of the block has the displacements fixed in the x–y plane. The bottom surface, on the contrary, is only fixed in vertical z direction. Due to symmetry, only one quarter of the whole geometry has been modelled. The
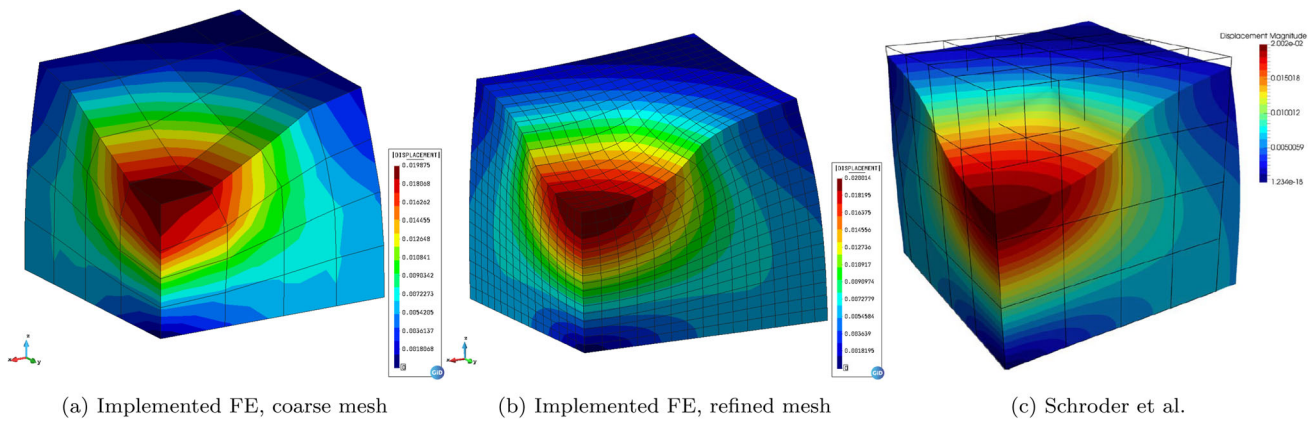
(a) Implemented FE, coarse mesh   (b) Implemented FE, refined mesh   (c) Schroder et al.

Fig. 3 Displacement field obtained with the implemented FE and the result provided in Schröder et al. [31]. Displacement units in m

Lamé parameters of the material are $\lambda = 499.92568$ MPa and $\mu = 1.61148$ MPa.

Figure 3 shows the results obtained with the implemented mixed *u-p* element together with the regularized Neo-Hookean hyperelastic law for a coarse and fine meshes. The results are in good agreement with the expected values given in Schröder et al. [31], which evidences that the locking effect due to incompressibility is circumvented, even when coarse meshes are used.

2.1.2 Fabric and steel fibres

In this work, the fibres are restricted to elastic behaviour, but its generalisation to orthotropy, plasticity or damage is straightforward and dealt by the rule of mixtures (Sect. 2.2). Since the fibres are typically submitted to moderate or relatively small strains, the compressible Neo-Hookean hyperelastic constitutive law has been used. In this case, the strain energy function used is the classical one given by:

$$\Psi = C_1(I_C^{(1)} - 3) - C_1 \ln(J) + \frac{C_2}{2}(J - 1)^2, \qquad (12)$$

from which the constitutive law and tangent tensor can be obtained [27].

2.2 Modelling composite materials in finite strains

To model the composite nature of tires, a modified version of the S-P RoM [15–18], which is an extension of the Mixing Theory, has been adapted to finite strains.

The evolution of classical homogenisation into the S-P RoM, allows to account for composites formed by two material constituents: fibre and matrix and considering different behaviours depending on the material orientation and loading. The iso-strain condition is only valid in the fibre direction (also called parallel behaviour). An iso-stress condition holds

for the orthogonal spatial directions of the fibre (serial direction), i.e.,

$$\text{Parallel behaviour}: \begin{cases} {}^c\mathbf{E}_P = {}^f\mathbf{E}_P = {}^m\mathbf{E}_P \\ {}^c\mathbf{S}_P = {}^f k\, {}^f\mathbf{S}_P + {}^m k\, {}^m\mathbf{S}_P \end{cases} \qquad (13)$$

$$\text{Serial behaviour}: \begin{cases} {}^c\mathbf{E}_S = {}^f k\, {}^f\mathbf{E}_S + {}^m k\, {}^m\mathbf{E}_S \\ {}^c\mathbf{S}_S = {}^f\mathbf{S}_S = {}^m\mathbf{S}_S \end{cases} \qquad (14)$$

where $\mathbf{E}$ is the Green-Lagrange strain tensor, $\mathbf{S}$ the second Piola-Kirchhoff stress tensor, k is the volumetric participation, c, f and m stand for composite, fibre and matrix, respectively, and P and S indicate parallel or serial behaviour, respectively. When dealing with oriented composite materials, it is always advisable to formulate the equations in the reference configuration, since rotations and differential volume changes can occur between the different material constituents. Fulfilling the set of equations at integration point level, described in Eqs. (13)–(14), defines a non-linear implicit set of equations (for non-linear constitutive laws) which resolution is detailed in [15–18, 32].

The SP-RoM ensures that the strains in the fibre direction are equal for the fibre and the matrix and, conversely, the stresses are in equilibrium in the serial direction. In standard composite materials, like reinforced concrete, FRP's, laminated materials, etc, the latter condition is easily achieved by the algorithm. However, if one of the material constituents stiffness is higher than 10,000 times that of the other material, a noticeable reduction of the numerical performance, or even non-convergence is exhibited. Since in tires the rubber material is notably more flexible than the steel/fabric cords, a modification of the SP-RoM has been developed, as described in the next section.

2.3 Particularisation of the SP-RoM for tire mechanics

In the modified version of the SP-RoM, the fibre is contributing to the composite stiffness only in the parallel direction whereas the matrix stiffness is considered only in the serial direction. In [15–18, 32] one can study how, by defining two fourth order tensors, one corresponding to the parallel direction $\mathbb{P}_p$ and the other one to the serial direction $\mathbb{P}_s$, the strain and stress tensors can be split in their parallel (p subscript) and serial (s subscript) counterparts as

$$\mathbf{E} = \mathbf{E}_p + \mathbf{E}_s \ , \quad \mathbf{S} = \mathbf{S}_p + \mathbf{S}_s, \tag{15}$$

being $\mathbf{E}_p$ the strain in the parallel direction, i.e.

$$\mathbf{E}_p = \mathbb{P}_p : \mathbf{E} \tag{16}$$

and $\mathbf{E}_s$ the strain in the serial direction:

$$\mathbf{E}_s = \mathbb{P}_s : \mathbf{E}. \tag{17}$$

The fourth order projector tensors in the serial and parallel direction are computed as

$$\mathbb{P}_p = \mathbf{N}_p \otimes \mathbf{N}_p \ \text{with} \ \mathbf{N}_p = \mathbf{e}_1 \otimes \mathbf{e}_1 \tag{18}$$

and

$$\mathbb{P}_s = \mathbf{I} - \mathbb{P}_p \tag{19}$$

where the director vector $\mathbf{e}_1$ determines the parallel behaviour (fibre direction), and $\mathbf{I}$ is the identity tensor. The stress state may be split analogously, by finding its parallel and serial parts using the 4th order tensors $\mathbb{P}_p$ and $\mathbb{P}_s$.

Knowing the constitutive laws used in the matrix material and the fibres, $^m\mathfrak{C}$ and $^f\mathfrak{C}$ respectively (Sects. 2.1.1 and 2.1.2), the composite stress used to compute the internal forces vector can be obtained as

$$^c\mathbf{S} = \underbrace{^fk(^f\mathbf{S}_p) + {}^mk(^m\mathbf{S}_p)}_{\text{Parallel behaviour}} + \underbrace{^m\mathbf{S}_s}_{\text{Serial behaviour}} \tag{20}$$

Equation (20) describes a composite material in which the parallel (fibre) direction behaviour is weighted between the fibre and matrix constitutive laws, whereas the serial behaviour is dominated by the matrix. Typically the direction of the fibre in $\mathbf{e}_1$ is unique (not mandatory), so the micro-buckling effect can be modelled by applying the Macaulay brackets to the parallel fibre contribution to the composite stress $\langle {}^m\mathbf{S}_p \rangle$. For the sake of completeness, the different contributions to the composite stress can be obtained as

$$^f\mathbf{S}_p = {}^f\mathfrak{C}(\mathbf{E}_p), \quad ^m\mathbf{S}_s = \mathbb{P}_s : {}^m\mathfrak{C}, \quad ^m\mathbf{S}_p = \mathbb{P}_p : {}^m\mathfrak{C}(\mathbf{E}). \tag{21}$$

The Sp-RoM add to the simple material constitutive laws (fibre and matrix) a certain measure of the strain, in this case the Green-Lagrange strain tensor $\mathbf{E}$. However, as described in Sects. 2.1.1 and 2.1.2, different versions of the Neo-Hookean hyperelastic laws are based on the right Cauchy-Green tensor $\mathbf{C}$. Hence, inside each constituent material law, an initial equivalent right Cauchy-Green tensor $\tilde{\mathbf{C}}$ is computed as $\tilde{\mathbf{C}} = 2\mathbf{E}_{RoM} + \mathbf{I}$, $\mathbf{E}_{RoM}$ being the strain provided by the SP-RoM [the input strain in Eq. (21)] and $\mathbf{I}$ the identity tensor.

With all these modifications to the standard SP-RoM, one can run large strain composite simulations accounting for incompresibility and high stiffness differences between the material constituents in an efficient and accurate way.

2.4 Fibre orientation and multi-layer materials

In the previous section we showed how one can numerically treat fibre reinforced composite materials using the SP-RoM and its particularisation to tire materials. However, described in previous sections, tires are complex structures formed by several layers of differently oriented fibre reinforced rubber, (Fig. 4). In order to model this kind of multi-layered materials, an iso-strain condition is assumed for all the different layers existing within a FE (Fig. 5).

This means the same strain state is assumed for each layer, the strain twill be rotated to the layer local axes, and the stresses will be integrated according to the SP-RoM if the layer is fibre-reinforced, or to any constitutive model otherwise. Algorithm 1 describes schematically the operations followed to calculate the composite stress of a multi-layered material in finite strains. In the Algorithm, ^{lay}k corresponds to the volumetric participation of the corresponding layer with respect to the FE volume.

In Algorithm 1 one can see how an additional rotation at elemental level is performed. This is done to avoid the definition of multiple composite materials if, as in the case of tires, a cylindrical (or spherical) symmetry can be used.
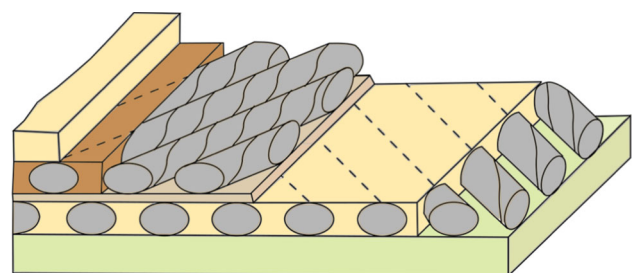

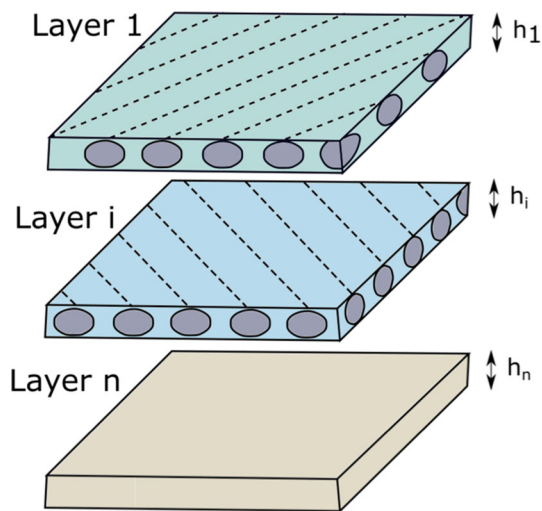**Fig. 4** Typical layered fibre-matrix type of material in tires

Fig. 5 Schematical separation when analysing more than one layer composite material, some of them can be fibre reinforced or simple material

After the stress is integrated at elemental or layer level, the rotations must transform to global axes when checking the equilibrium of the structure.

Algorithm 1 Multi-layered composite material constitutive law integration.

procedure $\rightarrow$ INSIDE INTEGRATION POINT LOOP WITHIN THE ELEMENT.
     Rotate $\mathbf{F}$ and/or strain $\mathbf{E}$ to elemental local axes $\rightarrow {}^{c}\mathbf{E}_{loc}$
     for layer **do**
         Rotate local elemental strain $\mathbf{E}_{loc}$ to layer local axes $\rightarrow \mathbf{E}_{lay,loc}$
         Integrate the constitutive law of the layer, simple material or SP-RoM algorithm $\rightarrow \mathbf{S}_{lay,loc}$
         Rotate layer strain and stresses to global layer axes, $\rightarrow \mathbf{S}_{lay,glob}$
     Compute composite stress ${}^{c}\mathbf{S} = \sum_{layer=0}^{n} {}^{lay}k\, \mathbf{S}_{lay,glob}$
     Rotate $\mathbf{F}$, strain and stress to elemental global axes $\rightarrow {}^{c}\mathbf{S}_{glob}$

---

3 Frictional computational contact mechanics

3.1 Introduction

This section details the derivation of the frictional *Mortar* contact condition formulation with *Augmented Dual Lagrange Multiplier*, presented in Mataix et al. [19], which is based mainly on the work of Popp [33, 34] and Gitterle [35], Cavalieri and Cardona [36, 37] and Yastrebov [38, 39], among others [40–42].

Contact mechanics problems are based on the Initial Boundary Value Problem (IBVP) of *non-linear* solid mechanics and *unilateral* contact constraints (Fig. 6). Unilateral contact leads to a constrained minimisation problem with inequality constraints, or more generally to so-called

variational inequalities. Both frictionless and frictional contact can either be formulated as variational inequalities with a constrained solution or as saddle point problems based on *Lagrange* multipliers; the last option has been the one adopted in this case.

The motivation for dual *Lagrange* multipliers [43, 44] lies in the fact that an extension of the master side basis functions to the slave side of the interface has a global support for standard *Lagrange* multipliers.

3.2 Strong formulation

In order to facilitate the understanding of the developments proposed, we define first place the frictionless problem and later introduce the frictional one. For the frictional case, the part relative to the solutions spaces is the same as the one presented for the frictionless case, as well as the balance of linear momentum (22).

3.2.1 Frictionless contact

On each subdomain Ω_0^i, the IBVP of finite deformation elastodynamics needs to be satisfied, viz Eq. (22). Here we are adding the Boundary Condition (BC) terms to the linear form and splitting in two different domains ($i = 1, 2$) the problem. This includes the *Dirichlet* BC in (22b), the *Neumann* BC from (22c) and the initial BC defined in (22d) and (22e).

$$\nabla \cdot \boldsymbol{\sigma}^i + \mathbf{b}^i = \rho^i \ddot{\mathbf{u}}^i \text{ in } \Omega^i \times [0, T] \tag{22a}$$
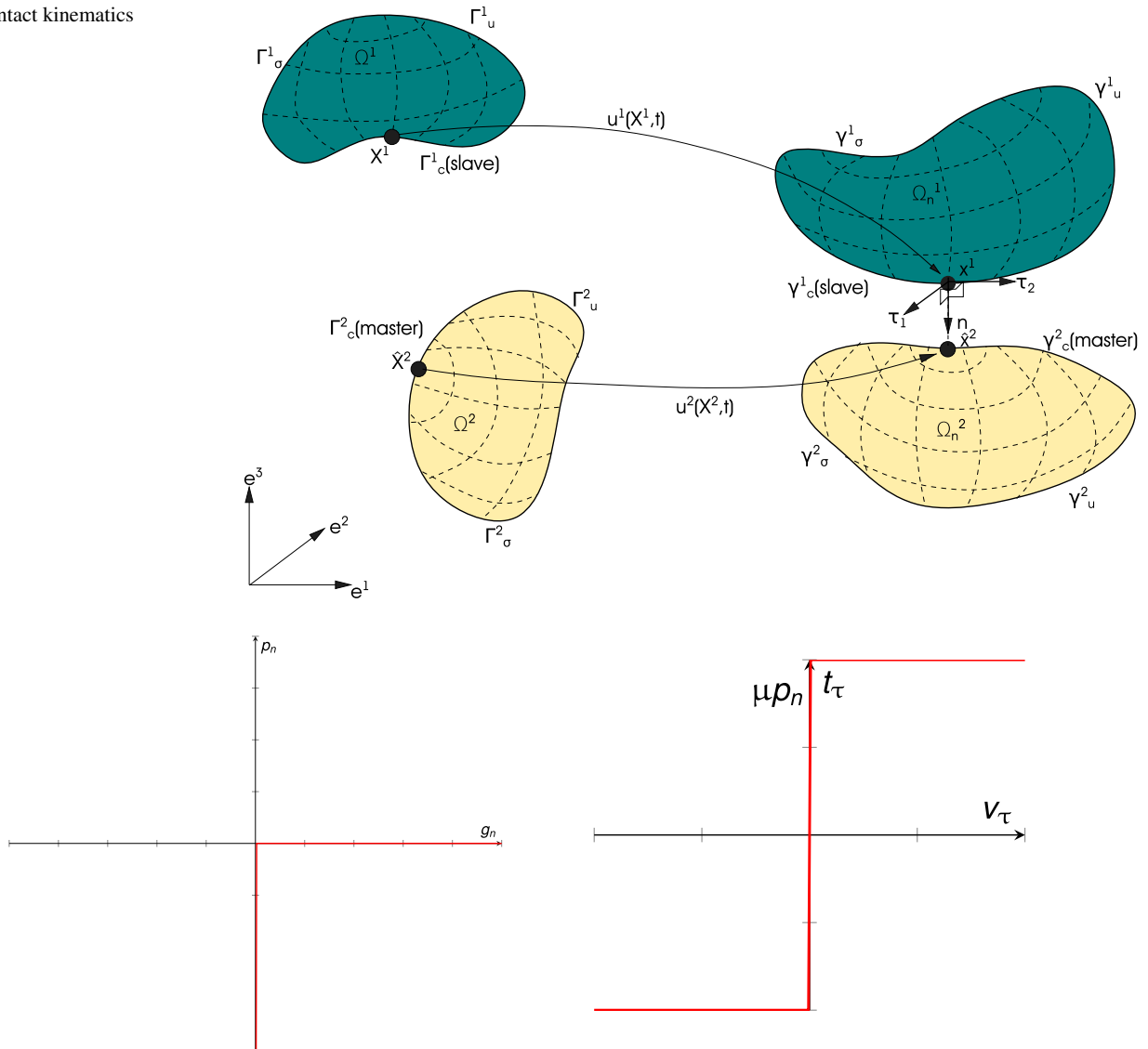
$$\mathbf{u}^i = \mathbf{u}^i \text{ on } \Gamma_u^i \times [0, T] \tag{22b}$$

$$\boldsymbol{\sigma}^i \cdot \mathbf{n}^i = \mathbf{t}^i \text{ on } \Gamma_\sigma^i \times [0, T] \tag{22c}$$

$$\mathbf{u}^i \left(\mathbf{X}^i, 0 \right) = \mathbf{u}_0^i \left(\mathbf{X}^i \right) \text{ in } \Omega_0^i \tag{22d}$$

$$\dot{\mathbf{u}}^i \left(\mathbf{X}^i, 0 \right) = \dot{\mathbf{u}}_0^i \left(\mathbf{X}^i \right) \text{ in } \Omega_0^i \tag{22e}$$

Fig. 6 Contact kinematics

(a) **KKT** conditions of non-penetration.

(b) *Coulomb's* schematic depiction of frictional contact

Fig. 7 Contact conditions

The contact constraints in the normal direction are typically expressed in the form of *Hertz-Signorini-Moreau* conditions as given in Eq. (23), and Fig. 7a. In optimisation theory these conditions are denominated usually as Karush-Kuhn-Tucker (KKT).

The weak formulation expresses the balance of linear momentum for the unilateral contact problem at the interface Γ_c^i. A Lagrange multiplier vector field λ_n is introduced, thus setting the basis for a mixed variational approach. Unilateral contact constraints are typically formulated (and later

also numerically evaluated) in the current configuration as

$$g_n \geq 0, \; p_n \leq 0, \; p_n g_n = 0 \text{ on } \Gamma_c^i \times [0, T] \qquad (23)$$

3.2.2 Frictional contact

Friction combines the interactions of elastic and plastic deformations at the contact interface, interaction with wear particles, micro-fractures, excitation of electrons, etc. The most commonly used friction model is based on *Coulomb's*

law (Fig. 7b). It can be defined as

$$\phi_{co} := \|\mathbf{t}_{co}^\tau\| - \mu\|p_n\| \le 0 \tag{24a}$$

$$\mathbf{v}_{\tau,rel}(\mathbf{X}^1, t) + \beta\mathbf{t}_{co}^\tau = \mathbf{0} \tag{24b}$$

$$\beta \ge 0 \tag{24c}$$

$$\phi_{co}\beta = 0 \tag{24d}$$

being μ the friction coefficient, and β the velocity-traction ratio. Equation (24a) requires the magnitude of the tangential stress vector to not exceed the product of the coefficient of friction and the normal contact pressure. When the tangential stress is less than the *Coulomb* limit ($\phi_{co} < 0$), the continuity equation (24d) forces β to be zero and, accordingly, the tangential relative velocity to be zero. This is called stick state. When the tangential stress is at the *Coulomb* limit ($\phi_{co} = 0$)), β may be greater than zero in (24d) and therefore the tangential stress is forced to oppose the relative tangential velocity in (24b),inducing the slip state.

The tangent direction $\boldsymbol{\tau}$ is defined as the complementary direction to the normal vector $\mathbf{n}$. The expression of $\boldsymbol{\tau}$ and the tangent Lagrange multiplier $\boldsymbol{\lambda}_\tau$ are given by

$$\boldsymbol{\tau} = \mathbf{I} - \mathbf{n} \otimes \mathbf{n} \tag{25a}$$

$$\boldsymbol{\lambda}_\tau = \boldsymbol{\lambda} - \mathbf{n}\lambda_n. \tag{25b}$$

3.3 Weak formulation

As in previous sections, the introduction of the weak formulation of the IBVP has been split into the frictionless and frictional cases.

3.3.1 Frictionless formulation

In this work we use the Augmented Lagrangian method applied to contact problems with friction proposed by Pietrzak and Curnier [45]. It is based on a reformulation of the contact and friction laws into a system of equations without inequalities. This overcomes the saddle point problem of the standard Lagrange multiplier. The resulting *Lagrangian* ($\mathcal{L}$) can be seen as a combination of the standard LM *Lagrangian* and the penalty approach. In order to avoid additional symbols we will introduce this method considering a scalar *Lagrange* multiplier, instead of a vector one, so we avoid the need to add a multiplication to the normal vector in each expression.

The functional related to the contact ($\mathcal{L}_{co}(\mathbf{u}, \lambda_n) = \mathcal{L}_{\mathcal{V}co} + \mathcal{L}_\mathcal{M}$) can be defined as

$$\mathcal{L}_{co}(\mathbf{u}, \lambda_n) = \int_{\Gamma_c^1} k\lambda_n \cdot g_n + \frac{\varepsilon}{2}g_n^2 - \frac{1}{2\varepsilon}\langle k\lambda_n + \varepsilon g_n\rangle^2 \mathrm{d}\Gamma_{co}^i \tag{26}$$

where ε is a positive penalty parameter, k is a positive scale factor, and $\langle\rangle$ is the *Macaulay* bracket operator, which is defined as:

$$\langle x\rangle = \begin{cases} x & x \ge 0 \\ 0 & x < 0 \end{cases} \tag{27}$$

This contact functional is $\mathcal{C}^1$ differentiable *saddle-point*, as shown in Fig. 8a. The solution is obtained as the set of values that render this functional stationary.

The functional of Eq. (26) can be split in two different terms, as (28). In Eq. (28) $k\lambda_n + \varepsilon g_n \le 0$ defines the contact zone and $k\lambda_n + \varepsilon g_n > 0$ the gap zone.

$$\mathcal{L}_{co}(\mathbf{u}, \lambda_n) = \int_{\Gamma_c^1} \begin{cases} k\lambda_n \cdot g_n + \frac{\varepsilon}{2}g_n^2\mathrm{d}\Gamma_{co}^i & \text{if } k\lambda_n + \varepsilon g_n \le 0 \\ -\frac{k}{2\varepsilon}\lambda_n^2 & \text{if } k\lambda_n + \varepsilon g_n > 0 \end{cases} \mathrm{d}\Gamma_{co}^1 \tag{28}$$

Finally, we can differentiate Eq. (28) to obtain the variational form, where we have defined the augmented normal pressure $\bar{\lambda}_n = k\lambda_n + \varepsilon g_n$:

$$\delta\mathcal{L}_{co}(\mathbf{u}, \lambda_n) = \int_{\Gamma_c^1} \begin{cases} \bar{\lambda}_n \cdot \delta g_n + kg_n\delta\lambda_n & \text{if } \bar{\lambda}_n \le 0 \\ -\frac{k^2}{\varepsilon}\lambda_n\delta\lambda_n & \text{if } \bar{\lambda}_n > 0 \end{cases} \mathrm{d}\Gamma_{co}^1 \tag{29}$$

The functional of Eq. (29) makes that the system obtained varies if the nodes are present in the contact zone or in the gap zone.

Cartesian Components of Lagrange multiplier

In order to be able to statically condense the resulting system of equations, Cartesian components LM are employed. Additionally, the Cartesian components LM are more consistent with the frictional formulation shown later. This is done by considering properties from the dual *Lagrange* multiplier approach, which is detailed in Appendix A.1.

The main modification consists in the replacement of the contact pressure LM, or λ_n, by a LM defined in the *Cartesian* components, represented as $\boldsymbol{\lambda}$, where the normal components (λ_n) are different or equal to zero, and the tangential ones ($\boldsymbol{\lambda}_\tau$) are always zero (in the frictionless scenario). This can be summarised as
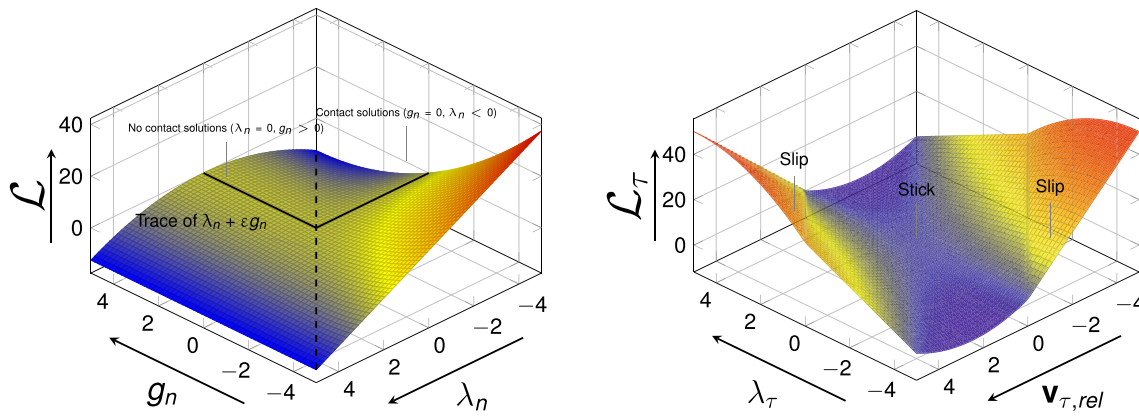
(a) Frictionless contact locus. Corresponding to (29)

(b) Frictional contact locus. Corresponding to (35b)

Fig. 8 Augmented Lagrangian function for the contact problem

$$\begin{cases} \lambda_n = \mathbf{n} \cdot \boldsymbol{\lambda} \\ \boldsymbol{\lambda}_\tau = \boldsymbol{\lambda} - \mathbf{n} \cdot (\mathbf{n} \cdot \boldsymbol{\lambda}) = \mathbf{0} \end{cases} \tag{30}$$

Cartesian components ALM Taking as base the solution presented in Sect. 3.3.1, and the modifications introduced in the previous section, it is required to define the Augmented LM by Cartesian components as

$$\bar{\boldsymbol{\lambda}} = k\boldsymbol{\lambda} + \varepsilon\mathbf{n}g_n. \tag{31}$$

Taking this into account, for the contact contributions of the potential and its variation, Eq. (28) can be reformulated as:

$$\mathcal{L}_{co}(\mathbf{u}, \boldsymbol{\lambda}) = \int_{\Gamma_c^1} \begin{cases} \bar{\lambda}_n \cdot \left(\mathbf{u}^1 - \mathbf{u}^2\right) + \frac{\varepsilon}{2} g_n^2 \mathrm{d}\Gamma_{co}^i & \text{if } \bar{\lambda}_n \leq 0 \\ -\frac{k}{2\varepsilon} \boldsymbol{\lambda}^2 & \text{if } \bar{\lambda}_n > 0 \end{cases} \mathrm{d}\Gamma_{co}^1 \tag{32a}$$

$$\delta\mathcal{L}_{co}(\mathbf{u}, \boldsymbol{\lambda}) = \int_{\Gamma_c^1} \begin{cases} \bar{\lambda}_n \cdot \left(\delta\mathbf{u}^1 - \delta\mathbf{u}^2\right) + kg_n\delta\boldsymbol{\lambda} \cdot \mathbf{n} & \text{if } \bar{\lambda}_n \leq 0 \\ -\frac{k^2}{\varepsilon} \boldsymbol{\lambda}\delta\boldsymbol{\lambda} & \text{if } \bar{\lambda}_n > 0 \end{cases} \mathrm{d}\Gamma_{co}^1 \tag{32b}$$

$$\delta\mathcal{L}_\lambda(\mathbf{u}, \boldsymbol{\lambda}) = \int_{\Gamma_c^1} k(\mathbf{n} \cdot \delta\boldsymbol{\lambda}) \cdot g_n - \frac{k^2}{\varepsilon}$$
$$(\boldsymbol{\lambda} - \mathbf{n} \cdot \boldsymbol{\lambda})(\delta\boldsymbol{\lambda} - \mathbf{n} \cdot \delta\boldsymbol{\lambda})\mathrm{d}\Gamma_{co}^1 \tag{32c}$$

where $\lambda_n = k(\mathbf{n} \cdot \boldsymbol{\lambda}) + \varepsilon g_n$ notation has been used.

3.3.2 Frictional formulation

Augmented Lagrangian Method with Friction The ALM method to solve contact problems with friction is very similar to the frictionless case as initially proposed by Pietrzak and Curnier [45]. Additionally to these references, the work of Cardona [46] and Yastrebov [38] have been considered here. Focusing in the contact functional ($\mathcal{L}_{co}(\mathbf{u}, \boldsymbol{\lambda}) = \mathcal{L}_{\mathcal{V}_{co}} + \mathcal{L}_{\mathcal{M}}$), one can rewrite it as

$$\mathcal{L}_{co}(\mathbf{u}, \boldsymbol{\lambda}) = \int_{\Gamma_c^1} l_n + l_\tau \mathrm{d}\Gamma_{co}^i, \tag{33}$$

where l_n and l_τ are the corresponding parts of the *Augmented Lagrangian* formulation for the normal and tangent contributions respectively, given as

$$l_n(g_n, \lambda_n) = \begin{cases} \bar{\lambda}_n g_n - \frac{\varepsilon_n}{2} g_n^2, & \bar{\lambda}_n \leq 0, \text{ (Contact zone)} \\ -\frac{k^2}{2\varepsilon_n} \lambda_n^2, & \bar{\lambda}_n > 0, \text{ (Gap zone)} \end{cases} \tag{34a}$$

with $\bar{\lambda}_n = k\lambda_n + \varepsilon_n g_n$ being the augmented *Lagrange* multiplier for the normal direction, and

$$l_\tau(\mathbf{v}_{\tau, rel}, \boldsymbol{\lambda}_\tau) = \begin{cases} \begin{cases} \bar{\boldsymbol{\lambda}}_\tau \cdot \mathbf{v}_{\tau, rel} - \frac{\varepsilon_\tau}{2} \mathbf{v}_{\tau, rel} \cdot \mathbf{v}_{\tau, rel} & , \|\bar{\boldsymbol{\lambda}}_\tau\| \leq -\mu\bar{\lambda}_n, \text{ stick} \\ -\frac{1}{2\varepsilon_\tau}\left(k^2\boldsymbol{\lambda}_\tau \cdot \boldsymbol{\lambda}_\tau + 2\mu\bar{\lambda}_n\|\boldsymbol{\lambda}_\tau\| + \mu^2\bar{\lambda}_n^2\right) & , \|\bar{\boldsymbol{\lambda}}_\tau\| > -\mu\bar{\lambda}_n, \text{ slip} \end{cases} & , \bar{\lambda}_n \leq 0, \text{ (Contact zone)} \\ -\frac{k^2}{2\varepsilon_\tau}\boldsymbol{\lambda}_\tau \cdot \boldsymbol{\lambda}_\tau & , \bar{\lambda}_n > 0, \text{ (Gap zone)} \end{cases} \tag{34b}$$

where $\bar{\lambda}_\tau = k\lambda_\tau + \varepsilon_\tau \mathbf{v}_{\tau,rel}$ stands as the augmented *Lagrange* multiplier for the tangent direction and ε_n and ε_τ are positive penalty parameters, both for normal and tangent direction and k is a positive scale factor. Using the *Macaulay* bracket operator, from Eq. (27), we can re-write the previous expressions as

$$l_n(g_n, \lambda_n) = \frac{1}{\varepsilon_n}\left(k^2\lambda_n^2 - \langle\bar{\lambda}_n\rangle^2\right), \tag{35a}$$

$$l_\tau(\mathbf{v}_{\tau,rel}, \lambda_\tau) = \frac{1}{\varepsilon_\tau}\left(k^2\lambda_\tau \cdot \lambda_\tau - \|\bar{\lambda}_\tau\|^2 - \langle\|\bar{\lambda}_\tau\| - \mu\| - \bar{\lambda}_n\|\rangle^2\right) \tag{35b}$$

This functional is a $\mathcal{C}^1$ differentiable *saddle-point*, as shown in Fig. 8b. As in the frictionless case, the solution does not depend on the value of parameters ε and k. Finally, we can derive Eq. (33) to obtain the variational form as

$$\delta\mathcal{L}_{co}(\mathbf{u}, \lambda) = \int_{\Gamma_c^1} \begin{cases} \bar{\lambda}_n \cdot \delta g_n + kg_n\delta\lambda_n + \bar{\lambda}_\tau \cdot \delta\mathbf{v}_{\tau,rel} + \mathbf{v}_{\tau,rel} \cdot \delta\bar{\lambda}_\tau & \text{if } \|\bar{\lambda}_\tau\| \leq -\mu\bar{\lambda}_n \text{ (Contact stick zone)} \\ \bar{\lambda}_n \cdot \delta g_n + kg_n\delta\lambda_n - \mu\bar{\lambda}_n\frac{\bar{\lambda}_\tau}{\|\bar{\lambda}_\tau\|}\delta\mathbf{v}_{\tau,rel} - \frac{k\lambda_\tau + \mu\bar{\lambda}_n\frac{\bar{\lambda}_\tau}{\|\bar{\lambda}_\tau\|}}{\varepsilon_\tau}\delta\lambda_\tau & \text{if } \|\bar{\lambda}_\tau\| > -\mu\bar{\lambda}_n \text{ (Contact slip zone)} \\ -\frac{k^2}{\varepsilon_n}\lambda_n\delta\lambda_n - \frac{k^2}{\varepsilon_\tau}\lambda_\tau\delta\lambda_\tau & \text{if } \bar{\lambda}_n > 0 \text{ (Gap zone)} \end{cases} \mathrm{d}\Gamma_{co}^i \tag{36}$$

The functional defined by Eq. (36) varies depending if the nodes are present in the contact zone (slip or stick) or in the gap zone. Hence, the system is not a priory known like in the frictionless but adding the stick/slip condition.

The discretization and its numerical integration of the different functionals can be studied in 1.

4 Numerical examples

We present a set of numerical examples to ensure the consistency and validity of the methodologies provided. The first example consists in a hyperelastic plug submitted to a confinement and frictional contact. The second example is a classical benchmark used for tire mechanics. This example, commonly named as "Grosch wheel", consists in a rubber wheel that is forced to rotate along his axis with different longitudinal miss-alignments, inducing frictional horizontal forces. Finally, a real Goodyear GT2 195/65R15 tire experiment is numerically reproduced.

4.1 Press fit

The problem consists of the numerical simulation of a press-fit process of a block in a channel according to [47, 48]. The geometric and material parameters are shown in Fig. 9, where only half of the domain is simulated due to symmetry. A *Neo-Hookean* compressible hyperelastic material is considered for both materials with the values from Table 1. With this

Table 1 Parameters considered for press fit

Body	Young modulus (Pa)	Poisson ratio	Friction coefficient
Die	21×10^9	0.32	0.1
Block	1×10^9	0.47	0.1

problem, it is possible to evaluate the behaviour of the contact element in a friction contact problem with large deformation and sliding.

The process is modelled by applying a non-homogeneous boundary displacement $u = 1000mm$ on the left face of the block. The height of the block is greater than the channel, imposing an initial penetration $\Delta initial = 1mm$ and consequently an initial contact stress. The first time step uses $u = 0mm$ and the program generates the normal stress necessary to the non-penetration condition and separates the bodies in contact. After this step, a non-homogeneous boundary condition $u = 1000mm$ is applied. We consider a plane strain state and an UL (*Updated Lagrangian*) formulation. Different result snapshots can be seen in Fig. 10 in which the Von-Mises stress contour fill is plotted. As expected, the friction induced by the contact of the plug against the walls deforms the hyperelastic material in the vertical direction (due to pressure) and some lateral distortion (due to the horizontal frictional forces). Quantitatively, Fig. 11 shows a very good agreement in terms of time evolution of the horizontal force needed to push the hyperelastic plug.

4.2 Grosch wheel

In this example, a rolling rubber wheel is studied. The geometry of the wheel can be seen in Fig. 12 (1680 hexahedral mixed elements for the rubber and 600 standard TL elements for the ground). The problem corresponds to the so-called Grosch wheel, widely used for standardised friction experiments of rubber [49–51]. The wheel has an outer radius of 40 mm, an inner radius of 17.5 mm and a thickness of 18 mm. The material properties are given in Table 2. The proposed mixed element has been used in the rubber material and standard TL elements at the rim and ground. Neo-Hookean hyperelastic constitutive laws have been used. The ground has been fixed at its lower surface whereas the Dirichlet boundary
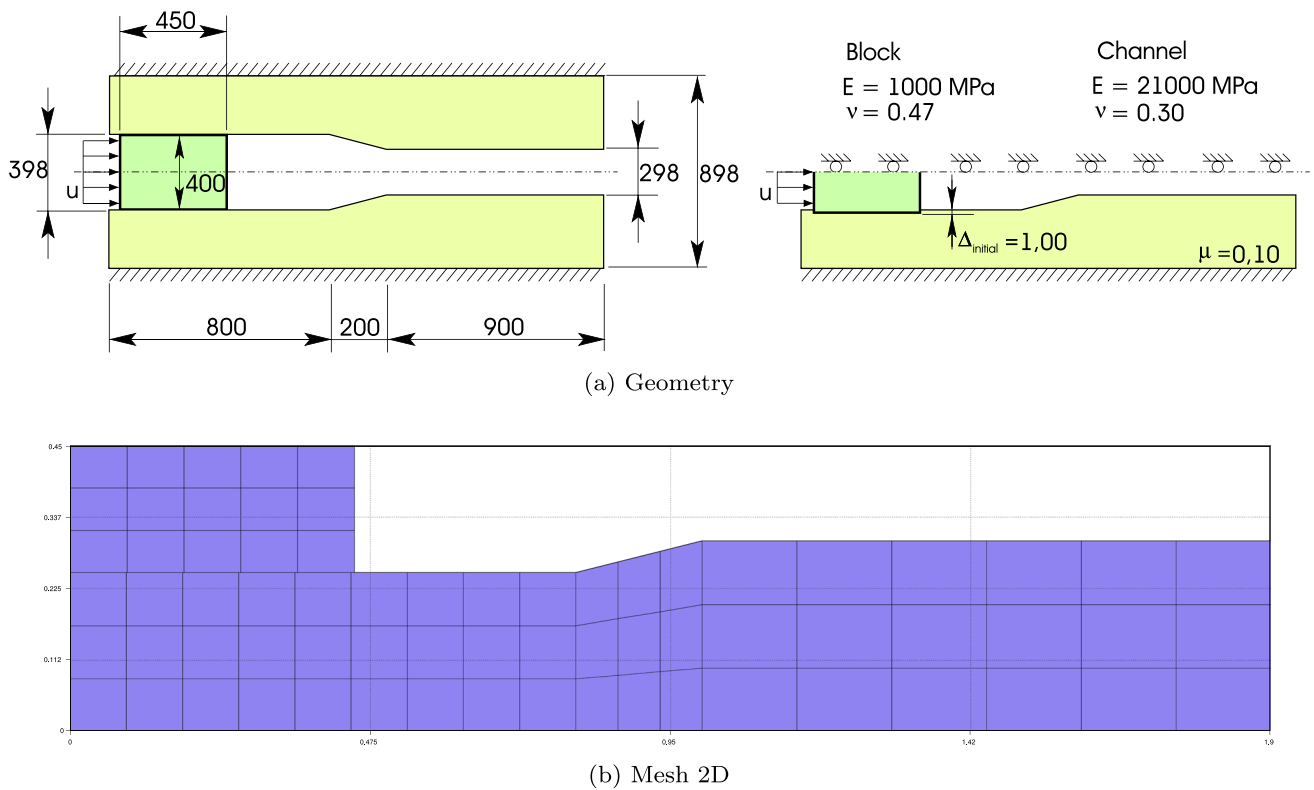
(a) Geometry

(b) Mesh 2D

Fig. 9 Press fit problem

(a) $t = 0.28s$

(b) $t = 0.56s$
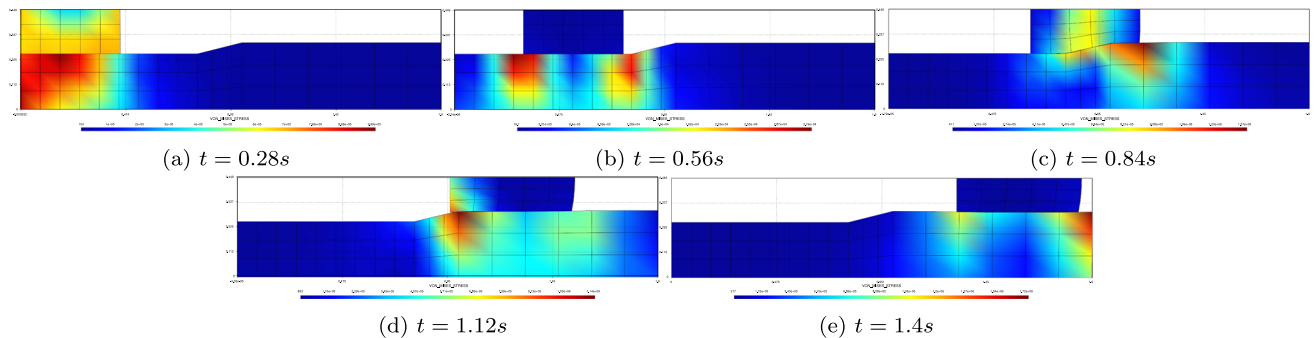
(c) $t = 0.84s$

(d) $t = 1.12s$

(e) $t = 1.4s$

Fig. 10 Press fit 2D solution. Von Mises stress contour fill. Units in [Pa]

conditions on the wheel have been applied at the cylindrical symmetry line at the centre of the rim material. Initially, the wheel is pressed 4 mm downwards and then the ground starts moving horizontally with different miss-alignments at a velocity of 2.5 mm/s, inducing horizontal frictional forces. As expected, the more miss-alignment, α, the more frictional forces are induced by the wheel.

Figure 13 shows the induced tangential pressures for different α angles. As expected, the bigger α is, the larger the tangential stresses induced. Since the material is highly flexible, one can see how the wheel gets deformed due to the friction against the ground. This effect is especially noticeable for $\alpha = 45$ deg, which after 6 s of simulation the wheel

gets totally distorted. As expected, for the $\alpha = 0$ deg case, the tangential stresses point inwards the wheel due to the Poisson effect. For the other angles, the tangential stresses are proportional and opposed to the advancing velocity.

Finally, the temporal evolution of the vertical and horizontal reaction forces can be studied in Fig. 14 for different α miss-alignments. As it can be seen, the vertical forces remain constant in all simulation regardless of the angle. However, the horizontal reaction tends to increase together with α. For the $\alpha = 45$ case, the tangential forces induce a distortion of the wheel in such a way that at $t = 6s$ the wheel contacts the ground with its lateral edge, inducing the simulation to be unstable.
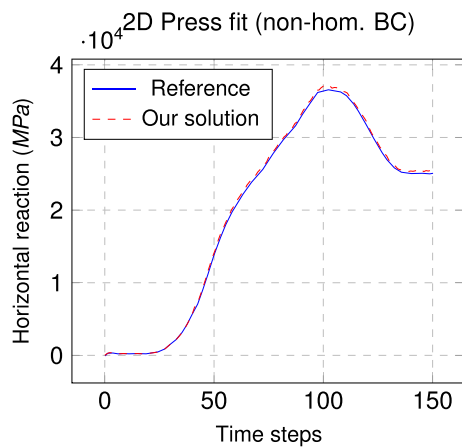
Fig. 11 Solution for 2D press fit compared with references [47, 48]

4.3 Pneumatic tire

In this section, the experimental results of a real Goodyear 195/65R15 tire obtained by Holscher et al. [24] are numerically reproduced. The tire has been inflated with different internal pressures (2, 2.5 and 3 bar) and then loaded monotonically. As expected, the deformation of the tire increases non-linearly with load and strongly depends on the internal pressure. A schematical view of the geometry can be seen in Fig. 15 in which the different layers of oriented steel/fibre cords can be identified. The material properties of the material constituents are given in Table 3 and the characteristics of the different composite materials involved can be seen in Table 4, inspired by the photographic information provided in Holscher et al. [24]. Table 4 shows the tread material is simply composed by one layer of rubber. The tire core is formed by three different layers, each one with its own fibre orientation and modelled by the SP-RoM combining a rubber matrix and steel/fibre cords. Finally, the sidewall is formed by one layer of composite material combining rubber and fibre cords. All the volumetric participations are estimated according to Holscher et al. [24]. The geometrical position

**Table 2** Parameters considered for the Grosch wheel example

Body	Young modulus (Pa)	Poisson ratio	Friction coefficient
Rubber	20×10^6	0.4995	1.0
Rim	2×10^{11}	0.29	–
Ground	2×10^{11}	0.29	1.0

of each composite material is depicted in Fig. 17. The friction coefficient has been chosen to be 0.5. As Fig. 17 shows, the tire thickness of the tire has been discretized with four mixed FE. The FE mesh used can be seen in Fig. 16. Mixed elements have been used for the tire composite materials and standard TL elements for modelling the ground.

Once the tire has been pressurised (2, 2.5 and 3 bar), a downwards boundary condition is applied on the bead material, acting as an equivalent rim, pressing the tire against the ground up to a vertical reaction of 4 kN. The deformed shape of the tire before and after the application of the internal pressure and after making contact against the ground are depicted in Fig. 18. The contact surface and the induced normal pressure can be seen in Fig. 19, for two vertical reactions of 2 kN and 4 kN, respectively.

A comparison between the experiment described in Holscher et al. [24] and the results of the simulation in terms of force-displacement evolution is depicted in Fig. 20. A very good agreement between the experimental and numerical results for all the different internal pressures studied have been obtained. This ensures that the material stiffness and the contact forces have been accurately estimated. Finally, Fig. 21 shows the tire profile for different conditions, comparing the simulated results and the experimental data. The similarity in tyre profile in all scenarios between the obtained and simulated results is excellent. This evidences that the flexibility of the material has been correctly reproduced with the methodologies presented in this work.

Fig. 12 Geometry and dimensions of the Grosch wheel analysed [49, 51]
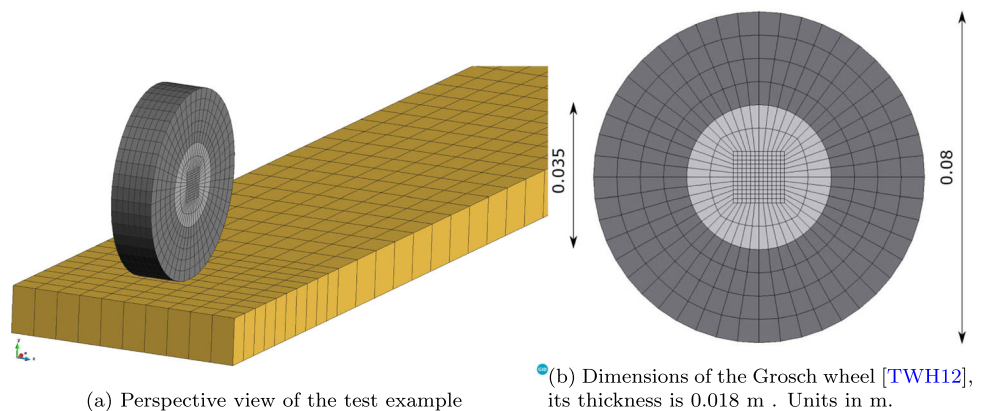
(a) Perspective view of the test example

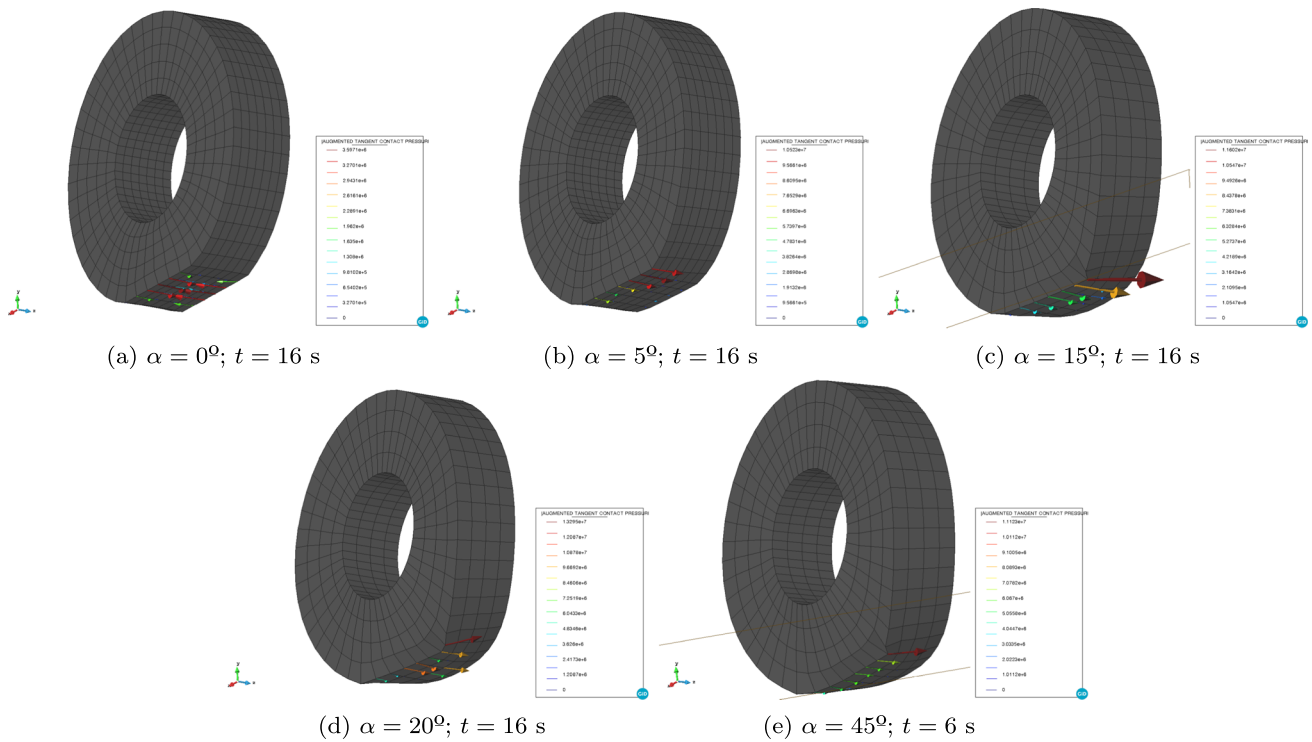(b) Dimensions of the Grosch wheel [TWH12], its thickness is 0.018 m . Units in m.

(a) $\alpha = 0^{\mathrm{o}}$; $t = 16$ s   (b) $\alpha = 5^{\mathrm{o}}$; $t = 16$ s   (c) $\alpha = 15^{\mathrm{o}}$; $t = 16$ s

(d) $\alpha = 20^{\mathrm{o}}$; $t = 16$ s   (e) $\alpha = 45^{\mathrm{o}}$; $t = 6$ s

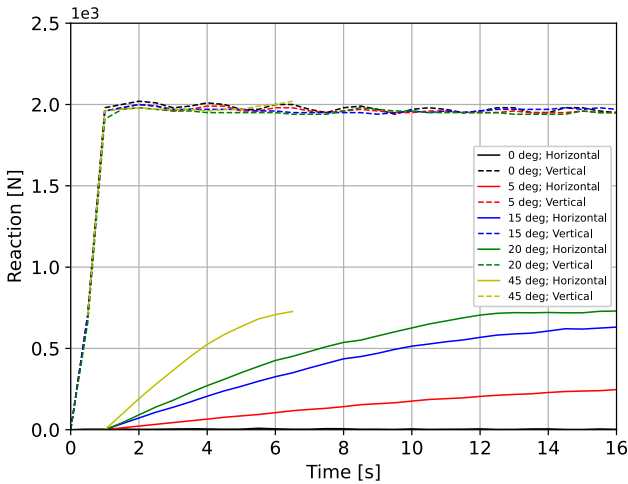**Fig. 13** Tangential frictional forces for different angle miss-alignments of the Grosch wheel

Fig. 14 Time evolution of the horizontal and vertical reaction for different longitudinal miss-alignments of the Grosch wheel

Table 3 Parameters considered for the simple materials for the tire example

Body	Young modulus [Pa]	Poisson ratio
Rubber (tread)	2.0×10^6	0.4995
Rubber (sidewall)	5.0×10^6	0.4995
Rubber (core)	30.0×10^6	0.4995
Steel belts	2.0×10^{11}	0.3
Cord ply	3.97×10^9	0.3

through the rubber and a large difference of stiffness inside the composite material. In addition, since the main purpose of tires is to ensure a proper adherence of the vehicle to the ground in contact. The proposed constitutive technology has been extended to account for frictional contact between deformable solids.

Each issue has been solved by:

5 Concluding remarks and future work

We have proposed a general framework for predicting the mechanical behaviour of highly complex composite structures. Indeed, the numerical analysis of tires implies solving several issues and non-linearities, namely, volumetric incompressibility and finite strains of the rubber-like material, large displacements and rotations of the geometry, composite material treatment and inclusion/orientation of the fibres

- *Incompressibility and large displacements* For tackling the incompressibility that rubber-like materials may exhibit, a standard mixed Total Lagrangian *u-p* element has been successfully used. In order to employ a more robust formulation, a mixed displacement-volumetric strain ($u - det(\mathbf{F})$) will be developed in the future in the large displacement framework starting from the work of Rossi et al. [52] in the small strain regime.
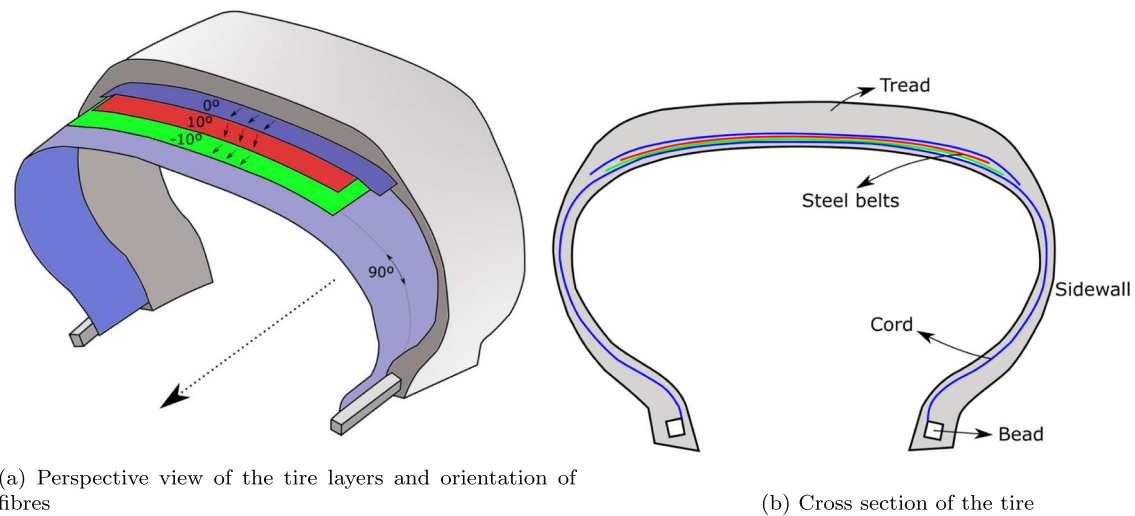
(a) Perspective view of the tire layers and orientation of fibres

(b) Cross section of the tire

Fig. 15 Schematical distribution of layers in the studied tire by Holscher et al [24]

- *Composite material treatment in finite strains* For efficiently modelling composite materials, a phenomenological homogenisation has been proposed: the serial-parallel rule of mixtures, which has been also extended to finite strains. With this technology, the mechanical behaviour of fibre-reinforced composite materials can be accurately reproduced since it distinguishes between the so-called parallel (direction of the fibre) and the serial (the remaining directions) response of the composite. In the standard SP-RoM, the global behaviour of the composite is obtained by iteratively solving an implicit system of equations. This procedure is generally very efficient but, when incompressibility and high flexibility of one constituent (rubber) is combined with a far stiffer and compressible material like steel fibres, a loss of performance or even divergence of the iterative strategy can occur. To circumvent this problem, a convenient modification of the standard SP-RoM has been developed in which the serial behaviour of the composite is dominated by the rubber, whereas in the parallel direction the different contributions of the rubber and steel/fibre cords are taken into account. With this simplification, the system of equations to be solved are explicit and the convergence of the constitutive problem is ensured with a noticeable reduction of the computational cost. In order to model different layers of fibre-reinforced composite materials, a classical rule of mixtures extended to finite strains has been implemented and used. The full tire example (Sect. 4.3), the proposed modified SP-RoM can efficiently and accurately reproduce the mechanical response of a real tire with different layers and orientation of fibre-reinforced rubber materials.

- *Frictional contact* For solving frictional contact problems, a state of the art DALMM combined with a Mortar method discretization was employed and validated. The proposed contact methodology is especially suited for implicit frameworks and it is totally consistent in terms

Table 4 Composite materials definition for each layer of the tire

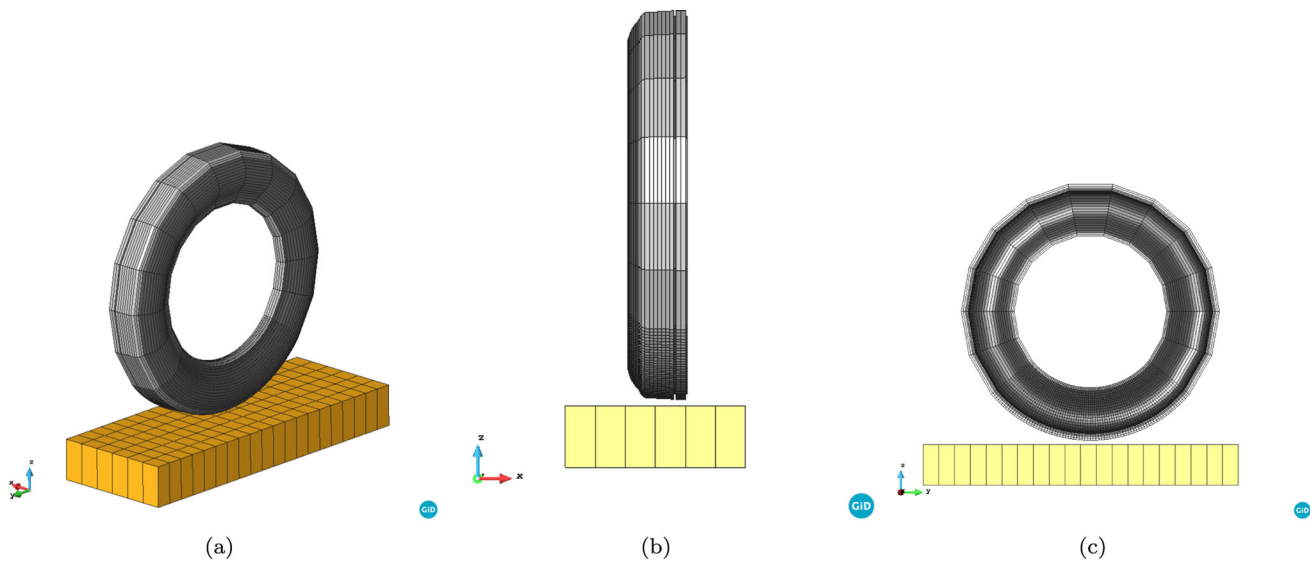| *Tread*				
Layer Id	Layer volumetric participation	Euler angles	Matrix material, Vol. participation	Fibre material, Vol. participation
1	1.0	(0,0,0)	Rubber (tread), 1.0	-
Steel/fibre composite (tire core)				
Layer Id	Layer volumetric participation	Euler angles	Matrix material, Vol. participation	Fibre material, Vol. participation
1	0.5	(0,0,0)	Rubber (core), 0.84	Fibre cords, 0.16
2	0.25	(0,20,0)	Rubber (core), 0.828	Steel belts, 0.172
3	0.5	(0,-20,0)	Rubber (core), 0.828	Steel belts, 0.172
Sidewall				
Layer Id	Layer volumetric participation	Euler angles	Matrix material, Vol. participation	Fibre material, Vol. participation
1	1.0	(0,0,0)	Rubber (sidewall), 0.62	Fibre cords, 0.38

Fig. 16 Different views of the Goodyear GT2 195/65R15 FE model, 212,325 nodes and 7560 linear hexahedral elements
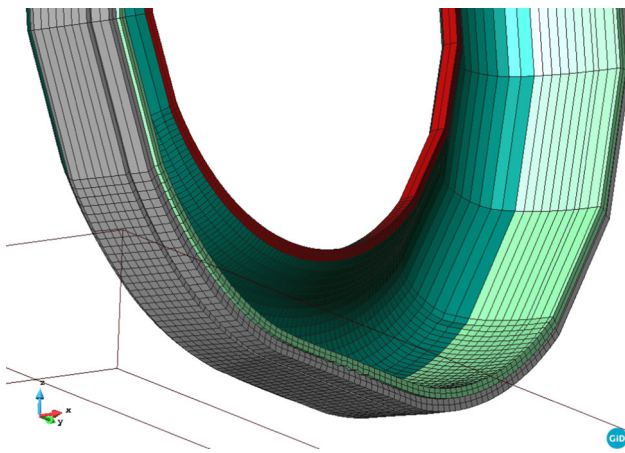

Fig. 17 Detail of the FE mesh used and the material distribution: bead material in red, tread in grey, sidewall in cyan and steel belt composite in green

of gap estimation, even when large sliding and displacements are expected. After studying the frictional forces and reactions retrieved from the conducted numerical examples and comparing them to the reference results, one

can ensure that the formulation and its implementation is correct, robust and variationally consistent. As far as this work is concerned, the friction coefficient is given as a known constant material property. This assumption is sufficient for many applications in structural mechanics; however, in the special case of rubber friction on rough surfaces, the resulting simplification is not entirely satisfied [53]. Generally, the rubber material undergoes large strains during contact, such that the frictional properties result for the main part from internal energy dissipation and not just from the combination of surfaces in contact. As it is apparent from experiments, the friction coefficient depends heavily on various parameters like sliding velocity, surface roughness, normal forces and temperature change, which are known only in the micro-scale. To solve this kind of problems in the future, a procedure proposed in Reinelt and Wriggers [53, 54] and Wagner et al. [55] will be followed in which a sequence of computations at different scales has to be performed in order to obtain the total friction law at the macro-scale for elastomer friction.
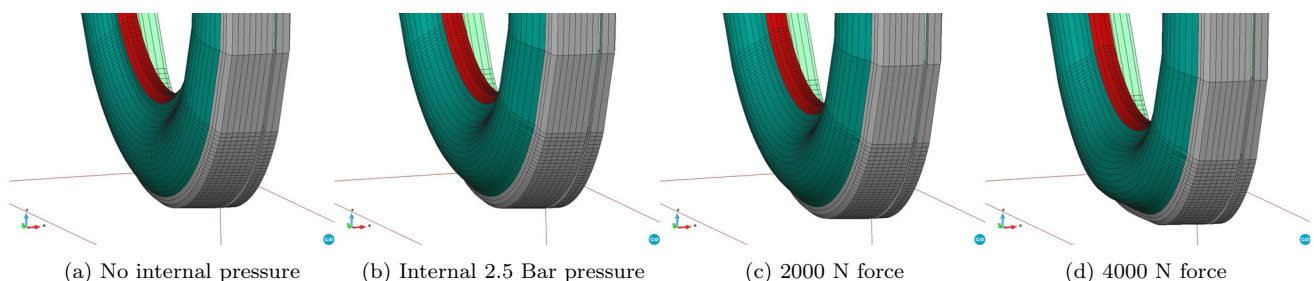

(a) No internal pressure (b) Internal 2.5 Bar pressure (c) 2000 N force (d) 4000 N force

Fig. 18 Deformed shape of the tire for different scenarios

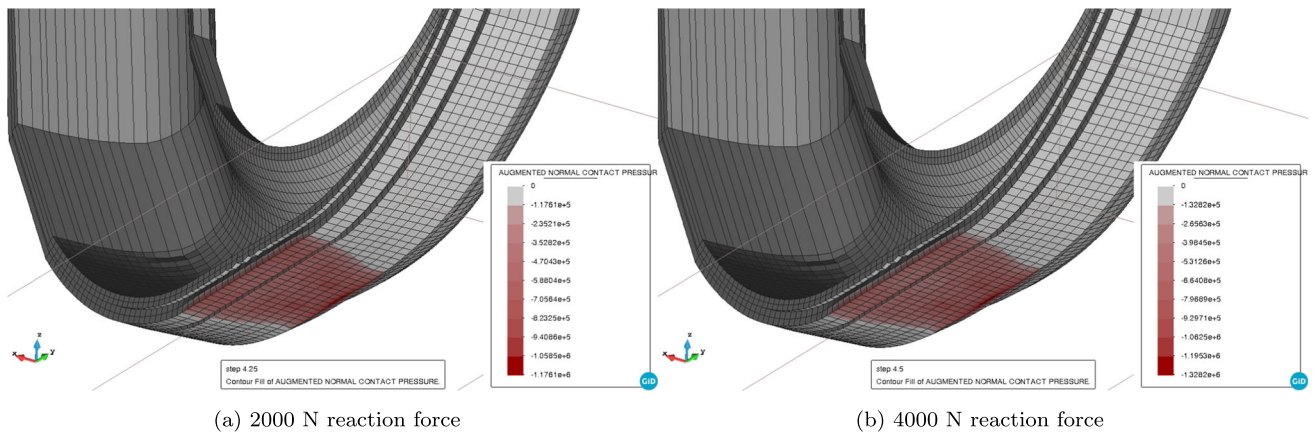(a) 2000 N reaction force   (b) 4000 N reaction force

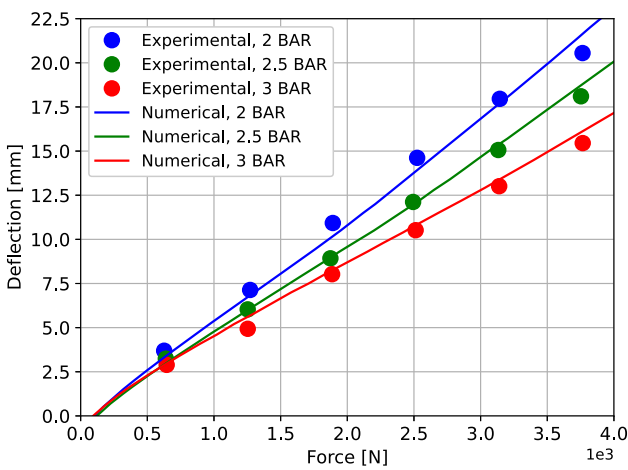**Fig. 19** Nodal contact pressure at different time seps, units in [Pa]

Fig. 20 Time evolution of the vertical reaction for different internal pressures, comparison with the experimental results provided in Holscher et al. [24]
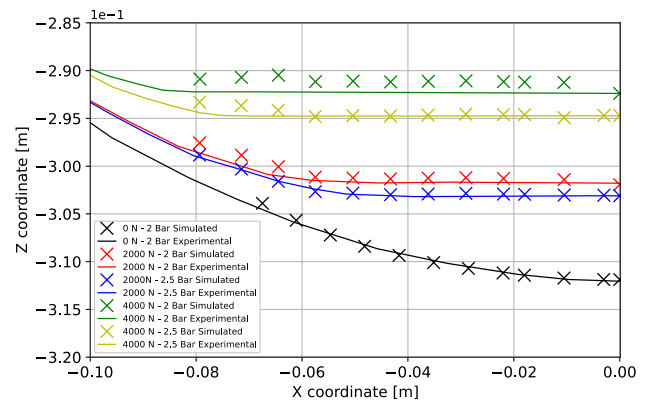

Fig. 21 Shape of the tire for different loads and internal pressures. Comparison of numerical results and experimental data from Holscher et al. [24]

Appendix 1: Augmented *Lagrange* multiplier parameters calibration

In this section we present a simple patch test [56] example, in order to show the influence of k and ε in the condition number (κ) of the stiffness matrix or LHS. We will see as the ε affects always negatively to κ, meanwhile k can improve or worsen depending on the range value considered.

The properties of the materials considered are listed in the Table 5. Taking Eq. (37) and assuming $h \approx 10$, our reference values will correspond with $\varepsilon = k = 100$. Additionally, the

Table 5 Parameters considered for ALM parameters calibration

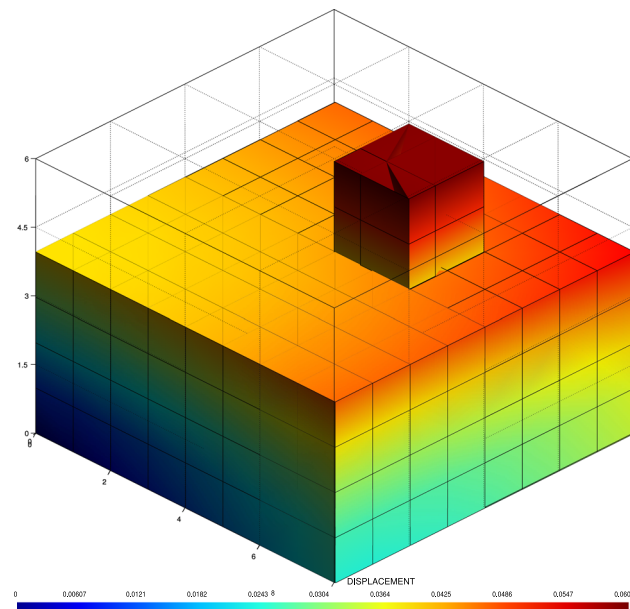| E Solid 1	ν Solid 1 [Pa]	E Solid 2 [Pa]	ν Solid 2
100	0.3	100	0.3

Fig. 22 Condition number study for the **ALM**

load considered at the top face of the punch block is equal to 1 Pa.

$$\varepsilon = k \approx 10 \frac{E_{mean}}{h_{mean}} \tag{37}$$

$$\kappa(A) = \frac{\sigma_{\max}(A)}{\sigma_{\min}(A)} \tag{38a}$$

$$\kappa(A) = \frac{|\lambda_{\max}(A)|}{|\lambda_{\min}(A)|} \tag{38b}$$

The condition number (κ) of a function measures it sensitivity with respect to the input arguments. A problem with a low condition number is said to be **well-conditioned**, while a problem with a high condition number is said to be **ill-conditioned**. In order to compute the corresponding κ one should evaluate the SVD, in order to compute the maximal and minimal singular values required in (38a). This expression can be simplified if A is **normal** ($A^*A = AA^*$); in this case we can simply compute κ considering the maximal and minimal eigenvalues as shown in (38b).[1] In Fig. 22 we can

see the proposed mesh for the 3D *Taylor* patch test, as well as the displacement solution of the problem.

Figure 23 represents graphically the results from Table 6. On the left, we plot the surface plot without any additional consideration, on the other hand, on the contour plot the k axis considers a logarithmic scale. In this continuous representation, it is possible to conclude several facts; foremost, is that the ε increases always the condition number, and the k may improve or not the κ depending on its value. Second of all, it is important to mention that, particularly in the right figure, the value estimated from Eq. (37), provides the best conditioning in overall.

Appendix 1.1: Discretisation and numerical integration

Dual Lagrange multipliers: The FE discretisation of the displacement field corresponds with the standard ones in finite element formulations. In addition, an adequate discretisation of the *Lagrange* multiplier vector λ is needed, and will be based on a discrete *Lagrange* multiplier space $\mathcal{M}_h$, being an approximation of $\mathcal{M}$. Thus, we can define the discrete *Lagrange* multiplier as in Eq. (39), with the shape functions Φ_j and the discrete nodal *Lagrange* multipliers λ_h:

$$\lambda_h = \sum_{i=1}^{m^1} \Phi_j\left(\xi^1, \eta^1\right)\lambda_j. \tag{39}$$

Details on how to define dual *Lagrange* multiplier shape functions Φ_j using the so-called bi-orthogonality relationship with the standard displacement shape functions N_k have first been presented in Wohlmuth [44]. A common notation of the bi-orthogonality condition is described in Eq. (40), where $\Gamma_{co,h}^1$ represents the discrete contact interface.

$$\int_{\Gamma_{co,h}^1} \Phi_j N_k^1 \mathrm{d}\Gamma_{co}^i = \delta_{jk} \int_{\Gamma_{co,h}^1} N_k^1 \mathrm{d}\Gamma_{co}^i, \; j, k = 1, \ldots, m^1 \tag{40}$$

Herein, δ_{jk} is the *Kronecker* delta, and the most common choice $m^1 = n^1$ is assumed. For practical reasons, the bi-orthogonality condition is typically applied locally on each slave element, represented with the index e, yielding Eq. (41), where m_e^1 represents the number of *Lagrange* multiplier nodes of the considered slave element.

$$\int_e \Phi_j N_k^1 \mathrm{d}e = \delta_{jk} \int_e N_k^1 \mathrm{d}e, \; j, k = 1, \ldots, m_e^1 \tag{41}$$

Footnote 1 continued

only in small systems. Another alternative if A is symmetric, then it is possible to compute the ratio between the max and min eigenvalues of A. In the case that A is not symmetric, it is possible to compute the max and min eigenvalues of $\sqrt{A^T A}$.
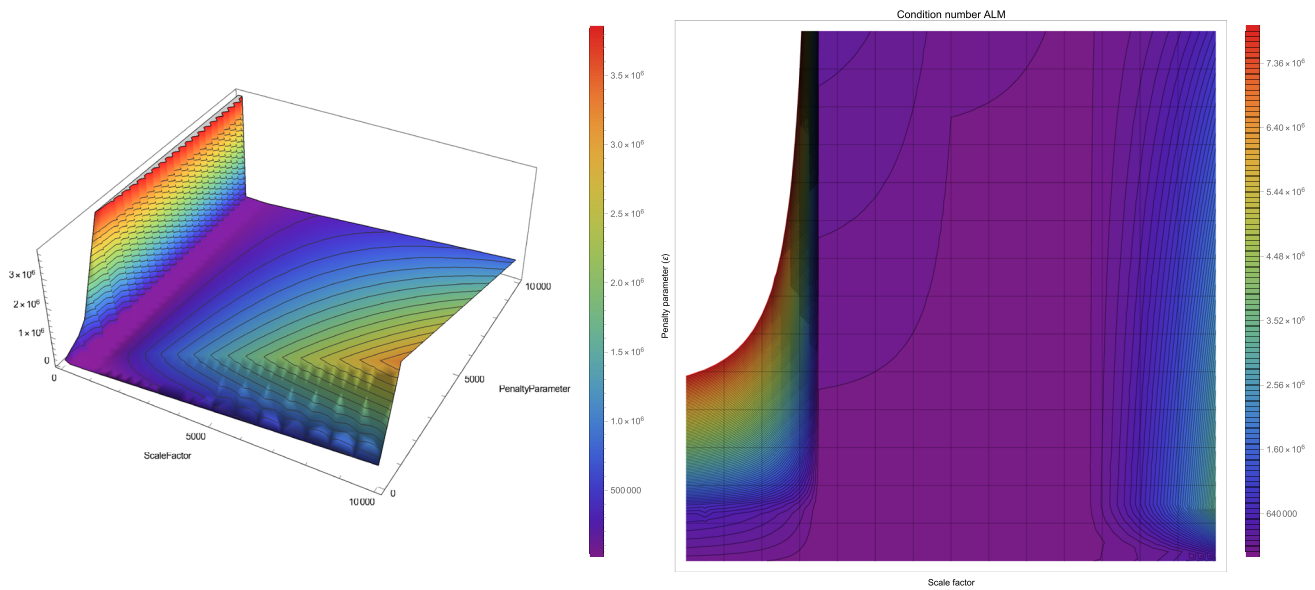
---

[1] We are considering SVD as it is the proper definition of the condition number, but in fact this is a very expensive operation and can be applied

Fig. 23 Condition number study graphic representation

Table 6 Results of numerical experiment for **ALM** parameters

k	ε	κ	k	ε	κ	k	ε	κ
1	1.00E−12	1.13E+05	10	1000	1.74E+04	1000	10	1.92E+04
1	1.00E−02	1.13E+05	10	10,000	2.69E+05	1000	100	1.81E+04
1	1	1.13E+05	100	1.00E−12	1.74E+04	1000	1000	3.14E+04
1	10	1.18E+05	100	1.00E−02	1.74E+04	1000	10,000	6.43E+04
1	100	1.63E+05	100	1	1.74E+04	10,000	1.00E−12	6.64E+05
1	1000	6.15E+05	100	10	1.74E+04	10,000	1.00E−02	6.63E+05
1	10,000	2.69E+07	**100**	**100**	**1.74E+04**	10,000	1	6.63E+05
10	1.00E−12	1.74E+04	100	1000	1.74E+04	10,000	10	6.63E+05
10	1.00E−02	1.74E+04	100	10,000	9.38E+04	10,000	100	3.53E+05
10	1	1.74E+04	1000	1.00E−12	6.60E+04	10,000	1000	3.26E+06
10	10	1.74E+04	1000	1.00E−02	6.60E+04	10,000	10,000	7.38E+05
10	100	1.74E+04	1000	1	5.75E+05			

Combining the biorthogonality condition in Eq. (41) and the partition of unity property of the dual shape functions, one can obtain:

$$\int_e \Phi_j \, de = \int_e N_j^1 \, de, \quad j = 1, \ldots, m_e^1. \tag{42}$$

The element-wise bi-orthogonality condition in Eq. (41) must be satisfied in the physical space, and not simply in the finite element parameter space. Consequently, a matrix system of size $m_e^1 \times m_e^1$ must be solved on each slave element. The first step for doing this is to introduce unknown linear coefficients a_{jk} such as:

$$\Phi_j(\xi, \eta) = a_{jk} N_k^1(\xi, \eta), \quad \mathbf{A}_e = [a_{jk}] \in \mathbb{R}^{m_e^1 \times m_e^1} \tag{43}$$

It can easily be verified that, as a second step, insertion of Eq. (43) into Eq. (41) yields the unknown coefficient matrix $\mathbf{A}_e$ as (44), where $J(\xi, \eta)$ is the slave *Jacobian* determinant.

$$
\begin{aligned}
\mathbf{A}_e &= \mathbf{D}_e \mathbf{M}_e^{-1} \\
\mathbf{D}_e &= [d_{jk}] \in \mathbb{R}^{m_e^1 \times m_e^1}, \; d_{jk} \\
&= \delta_{jk} \int_e N_k^1(\xi, \eta) J(\xi, \eta) \, de \\
\mathbf{M}_e &= [m_{jk}] \in \mathbb{R}^{m_e^1 \times m_e^1}, \; m_{jk} \\
&= \int_e N_j^1(\xi, \eta) N_k^1(\xi, \eta) J(\xi, \eta) \, de
\end{aligned}
\tag{44}
$$

Mortar operators:

Considering the discrete *Lagrange* multiplier defined in Eq. (39) we can rewrite $-\delta \mathcal{L}_{co,h}$ as in Eq. (45), where χ_h is

the interface mapping.

$$
\begin{aligned}
-\delta\mathcal{L}_{co,h} &= \sum_{j=1}^{m^1}\sum_{k=1}^{n^1}\boldsymbol{\lambda}_{nj}^T\left(\int_{\Gamma_{c,h}^1}\Phi_j N_k^1 \mathrm{d}\Gamma_{co}^i\right)\delta\mathbf{d}_{nk}^1 \\
&\quad -\sum_{j=1}^{m^1}\sum_{l=1}^{n^2}\boldsymbol{\lambda}_{nj}^T\left(\int_{\Gamma_{c,h}^1}\Phi_j\left(N_l^2\circ\chi_h\right)\mathrm{d}\Gamma_{co}^i\right)\delta\mathbf{d}_{nl}^2
\end{aligned}
\tag{45}
$$

Numerical integration of the mortar coupling terms is exclusively performed on the slave side $\Gamma_{c,h}$ of the interface. In Eq. (45), nodal blocks of the two mortar integral matrices commonly denoted as $\mathbf{D}_e$ and $\mathbf{M}_e$ can be identified. This leads to the following definitions:

$$
\begin{aligned}
\mathbf{D}[j,k] &= D_{jk}\mathbf{I}_{ndim} \\
&= \int_{\Gamma_{c,h}^1}\Phi_j N_k^1 \mathrm{d}\Gamma_{co}^i\mathbf{I}_{ndim},\ j=1,\ldots m^1,\ k=1,\ldots n^1 \\
&= \sum_{g=1}^{n_{gp}} w_g\phi_{gj}N_{gk}^1 J_g^1 \\
\mathbf{M}[j,l] &= M_{jl}\mathbf{I}_{ndim} \\
&= \int_{\Gamma_{c,h}^1}\Phi_j\left(N_l^2\circ\chi_h\right)\mathrm{d}\Gamma_{co}^i\mathbf{I}_{ndim},\ j=1,\ldots m^1,\ k=1,\ldots n^2 \\
&= \sum_{g=1}^{n_{gp}} w_g\phi_{gj}N_{gk}^2 J_g^1.
\end{aligned}
\tag{46}
$$

Discrete contact condition in tangential direction:

Following the same procedure for the normal direction we can obtain the part equivalent for the tangential direction. The most relevant thing to take into account before any definition is the concept of the relative velocity in the tangential direction $\mathbf{v}_{\tau,rel}$, where we will use for our definition the discrete form of the material velocity field $\dot{\mathbf{x}}^i$, which uses the same shape functions for interpolation as the $\mathbf{x}^i$. We can then define:

$$
\begin{aligned}
&\int_{\gamma_c^1}\mathbf{v}_{\tau,rel}\cdot(\delta\boldsymbol{\lambda}_\tau-\boldsymbol{\lambda}_\tau)d\gamma \\
&\approx \sum_{j=1}^{n_{slaves}}(\delta\boldsymbol{\lambda}_\tau-\boldsymbol{\lambda}_\tau)^T\boldsymbol{\tau}_j\left[\int_{\gamma_c^1}\Phi_j N_j^1 d\gamma\dot{\mathbf{x}}_j^1\right. \\
&\left.\quad -\sum_{l=1}^{n_{master}}\int_{\gamma_c^1}\Phi_j\left(N_l^2\cdot\xi\right)d\gamma\dot{\mathbf{x}}_l^2\right]\geq 0\,\forall\delta\boldsymbol{\lambda}\in\mathcal{M}(\boldsymbol{\lambda}).
\end{aligned}
\tag{47}
$$

One can express this equation using the mortar operators, see Sect. 1, what will allow the obtention of the following

expression (48). Where $\tilde{\mathbf{v}}_{\tau j}$ is the weighted relative velocity.

$$
\begin{aligned}
&\int_{\gamma_c^1}\mathbf{v}_{\tau,vel}\cdot(\delta\boldsymbol{\lambda}_\tau-\boldsymbol{\lambda}_\tau)d\gamma \approx \sum_{j=1}^{n_{slaves}}(\delta\boldsymbol{\lambda}_\tau-\boldsymbol{\lambda}_\tau)^T \\
&\boldsymbol{\tau}_j\left[\mathbf{D}_j\dot{\mathbf{x}}_j^1-\sum_{l=1}^{n_{master}}\mathbf{M}_l\dot{\mathbf{x}}_l^2\right]=\sum_{j=1}^{n_{slaves}}(\delta\boldsymbol{\lambda}_\tau-\boldsymbol{\lambda}_\tau)^T\tilde{\mathbf{v}}_{\tau j}\geq 0
\end{aligned}
\tag{48}
$$

Slip definition: An important aspect of a proper formulation of frictional laws in the finite sliding context is framed indifference [35, 42] of the rate measures involved. This affects the tangential relative velocity of the contacting bodies in the considered case of frictional contact. This assures that this quantity is unaffected by any rigid body motion which the two contacting bodies might experience at the instant of the question. Mathematically, this can be tested with formulating the tangential relative velocity in an alternative reference frame. Then in the current (mortar projected) instance, we must ensure frame indifference.

Working in the time continuous case first, one may readily show that the tangential component of the mortar projected tangential velocity is not frame indifferent (49a). Frame indifference is assessed by viewing the motion from another reference frame, denotes in the following by superscripts $\mathbf{c}(t)$, which can be related to the original spatial frame via (49b). Where $\mathbf{c}(t)$ is the relative rigid body translation between the original spatial frame and observer, while a relative rotation is produced by the proper orthogonal tensor, (49c). The frame indifferent relative tangential velocity should satisfy. However, by considering the effect of the transformation (49b) on (49a), it is readily seen that (49d).

$$
\tilde{\mathbf{v}}_\tau^{nononbj} = \boldsymbol{\tau}_j\left[\mathbf{D}_j\dot{\mathbf{x}}_j^1-\sum_{l=1}^{n_{master}}\mathbf{M}_l\dot{\mathbf{x}}_l^2\right]
\tag{49a}
$$

$$
\dot{\mathbf{x}}_l^{(1*)} = \mathbf{c}(t)+\mathbf{Q}(t)\dot{\mathbf{x}}_l^1
\tag{49b}
$$

$$
\tilde{\mathbf{v}}_\tau^* = \mathbf{Q}(t)\tilde{\mathbf{v}}_\tau
\tag{49c}
$$

$$
\tilde{\mathbf{v}}_\tau^{nonobj*} = \mathbf{Q}(t)\tilde{\mathbf{v}}_\tau^{nonobj}-\dot{\mathbf{Q}}(t)\left[\mathbf{D}_j\mathbf{x}_j^1-\sum_{l=1}^{n_{master}}\mathbf{M}_l\mathbf{x}_l^2\right]\cdot\boldsymbol{\tau}_j
\tag{49d}
$$

Because the term $\left[\mathbf{D}_j\mathbf{x}_j^1-\sum_{l=1}^{n_{master}}\mathbf{M}_l\mathbf{x}_l^2\right]\neq\mathbf{0}$ in general $\tilde{\mathbf{v}}_\tau^{nonobj*}$ does not satisfy the equation (49c), and thus some modifications are required to this relative velocity measure to assure material frame indifference. It is possible to restore the objectivity with the inclusion of the rate of a mortar projected distance between the two bodies, denoted as $\mathbf{g}$. Then
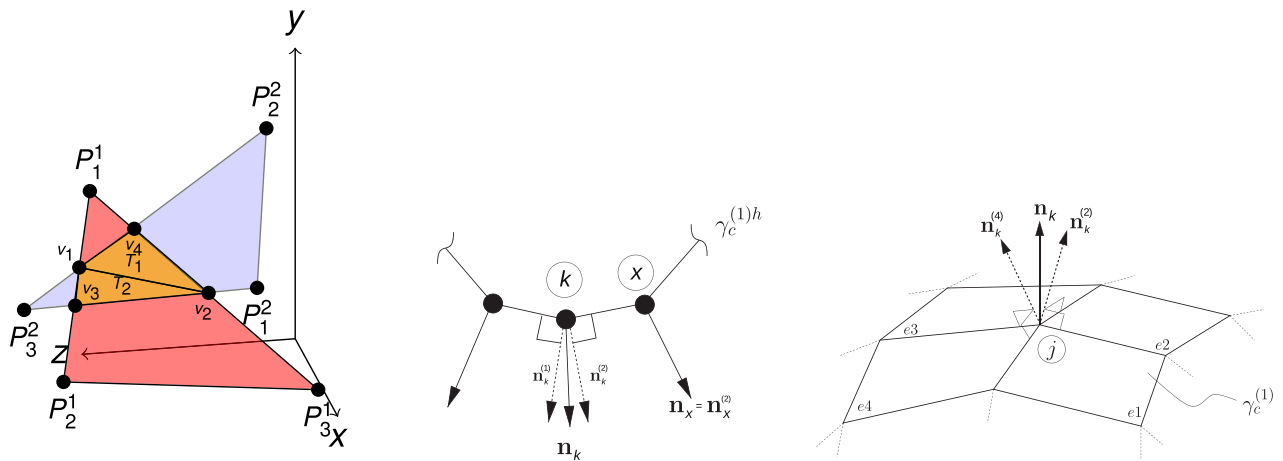
(a) Exact mortar segmentation in 3D

(b) Average normal definition

Fig. 24 Technical details

in consequence (50) is obtained.

$$\tilde{\mathbf{v}}_\tau = \boldsymbol{\tau}_j \left[\mathbf{D}_j \dot{\mathbf{x}}_j^1 - \sum_{l=1}^{n_{master}} \mathbf{M}_l \dot{\mathbf{x}}_l^2 - \dot{\mathbf{g}} \right] \tag{50}$$

We obtain an expression which retains the interpretation of the tangential relative velocity in the case where perfect sliding occurs (i.e. when $\dot{\mathbf{g}} = 0$), but which contains the modification necessary to make the velocity measure objectives under all conditions of contact. This is readily seen by using direct calculation to exactly re-express (50) as (51b), considering (51a).

$$\dot{\mathbf{g}} = \frac{\mathrm{d}}{\mathrm{d}t} \left[\dot{\mathbf{D}}_j \mathbf{x}_j^1 - \sum_{l=1}^{n_{master}} \dot{\mathbf{M}}_l \mathbf{x}_l^2 \right]$$
$$= \left[\dot{\mathbf{D}}_j \dot{\mathbf{x}}_j^1 - \sum_{l=1}^{n_{master}} \dot{\mathbf{M}}_l \dot{\mathbf{x}}_l^2 \right] + \left[\dot{\mathbf{D}}_j \mathbf{x}_j^1 - \sum_{l=1}^{n_{master}} \dot{\mathbf{M}}_l \mathbf{x}_l^2 \right] \tag{51a}$$

$$\tilde{\mathbf{v}}_\tau = \boldsymbol{\tau}_j \left[\dot{\mathbf{D}}_j \mathbf{x}_j^1 - \sum_{l=1}^{n_{master}} \dot{\mathbf{M}}_l \mathbf{x}_l^2 \right] \tag{51b}$$

The time derivatives of the mortar operators can be defined using any desired scheme, for example using the *backward Euler* (52) scheme as time discretisation.

$$\frac{\mathrm{d}(\cdot)}{\mathrm{d}t} \approx \frac{(\cdot)^{t+\Delta t} - (\cdot)^t}{\Delta t} \tag{52a}$$

$$\frac{\mathrm{d}\mathbf{D}}{\mathrm{d}t} \approx \frac{\mathbf{D}_l^{t+\Delta t} - \mathbf{D}_j^t}{\Delta t}, \quad \frac{\mathrm{d}\mathbf{M}}{\mathrm{d}t} \approx \frac{\mathbf{M}_l^{t+\Delta t} - \mathbf{M}_l^t}{\Delta t} \tag{52b}$$

With this we can define tangential relative velocity $\tilde{\mathbf{v}}_\tau$ as (53a), that multiplies by Δt gives us the nodal slip increment $\tilde{\mathbf{u}}_\tau$ (53b).

$$\tilde{\mathbf{v}}_\tau = \boldsymbol{\tau}_j \left[\frac{\mathbf{D}_j^{t+\Delta t} - \mathbf{D}_j^t}{\Delta t} \mathbf{x}_j^1 - \sum_{l=1}^{n_{master}} \frac{\mathbf{M}_l^{t+\Delta t} - \mathbf{M}_l^t}{\Delta t} \dot{\mathbf{x}}_l^2 \right] \tag{53a}$$

$$\tilde{\mathbf{u}}_\tau = \boldsymbol{\tau}_j \left[\left(\mathbf{D}_j^{t+\Delta t} - \mathbf{D}_j^t \right) \mathbf{x}_j^1 - \sum_{l=1}^{n_{master}} \left(\mathbf{M}_l^{t+\Delta t} - \mathbf{M}_l^t \right) \dot{\mathbf{x}}_l^2 \right] \tag{53b}$$

Appendix 1.2: Technical details

Exact integration In order to integrate the mortar operators defined in Section Appendix 1.1, one may take into account an exact integration, like seen in Fig. 24a in 3D, and the corresponding adaptation in 2D (see [33] for more details). In the case shown in Fig. 24a, a clipping and posterior tessellation algorithm must be implemented. These definitions have an important role in the definition and computation of the directional derivatives.

Normal definition In order to consider a smooth and continuous approximation of the normal field defined at the nodes of the FE mesh, an average normal definition has been used as shown in Fig. 24b. This definition must be taken into account in the definition of the consistent directional derivatives.

Appendix 1.3: Work-flow. Solution algorithm

The following section introduces the algorithm to be considered in order to solve the frictional contact problem. It is relevant to highlight the fact that this algorithm is related with

the semi-smooth strategy of the next section 4. The algorithm is presented in Algorithm 2.

For a frictional case, one needs to consider a quite complex active, which includes the active/inactive for the frictionless contact contribution, and the slip/stick state for the frictional contributions. In addition, it is needed to compute the corresponding residuals for these states, related with the LM solution, as well as the displacement. The last stated, means that the residual corresponding to the LM is divided into three different components, the relative to the normal direction, the relative to the tangent direction associated to the slip state, and finally the one obtained from the stick state. It is relevant to separate the residuals from the slip/stick states, as the magnitude orders from these components change greatly, and it may be difficult to achieve a convergence if mixing them. We remark the need to do this search at each time step in order to adapt to the evolution of the geometry.

Algorithm 2 Algorithm for the frictional contact problem

1: **procedure** ALGORITHM FOR THE FRICTIONAL CONTACT PROBLEM
2:     $t = 0$ and $i = 0$. Initialise the solution for $\mathbf{u}^0 = \mathbf{0}$
3:     In case of solving **LM** solution, Initialise the **LM** solution $\boldsymbol{\lambda}^0 = \mathbf{0}$
4:     Initialise the active set $\mathcal{A}_1^0$ and $\mathcal{I}_1^0$ such that $\mathcal{A}_1^0 \cup \mathcal{I}_1^0 = \mathcal{S}$ and $\mathcal{A}_1^0 \cap \mathcal{I}_1^0 = \emptyset$
5:     Initialise the slip/stick set $\mathcal{A}_{sl1}^0$ and $\mathcal{A}_{st1}^0$ such that $\mathcal{A}_{sl1}^0 \cup \mathcal{A}_{st1}^0 = \mathcal{A}_1^0$ and $\mathcal{A}_{sl1}^0 \cap \mathcal{A}_{st1}^0 = \emptyset$
6:     **while** $t < t_{end}$ **do**
7:         $t = t + \Delta t$ and $i = i + 1$. Initialise the increment of solution for $\Delta \mathbf{u}_1^i = \mathbf{0}$
8:         In case of solving **LM** solution, Initialise the **LM** increment of solution $\Delta \boldsymbol{\lambda}_1^i = \mathbf{0}$
9:         Search for potential contact pairs, and if required update the active set, respecting step 4
10:        We define the problem as not converged $conv = false$
11:        **while** $conv = false$ **do**
12:            Find the solution corresponding to the system
13:            Update the solution, so $\mathbf{u}_{n+1}^i = \mathbf{u}_n^i + \Delta \mathbf{u}_{n+1}^i$ and $\boldsymbol{\lambda}_{n+1}^i = \boldsymbol{\lambda}_n^i + \Delta \boldsymbol{\lambda}_{n+1}^i$
14:            Update the active set as in Eq. (54). The threshold is represented in (55).

$$\begin{aligned} \mathcal{I}_{n+1}^{i+1} &:= \left\{ j \in \mathcal{S} | threshold_{n+1}^{i+1} \geq 0 \right\} \\ \mathcal{A}_{n+1}^{i+1} &:= \left\{ j \in \mathcal{S} | threshold_{n+1}^{i+1} < 0 \right\} \end{aligned} \tag{54}$$

$$threshold = k\lambda_n + \epsilon \bar{g}_n \text{ or } k\mathbf{n} \cdot \boldsymbol{\lambda} + \epsilon \bar{g}_n \tag{55}$$

15:            Update the slip/stick set as in Eq. (56). To evaluate this, we require the frictional threshold $\mathscr{F}$, considering *Coulomb*'s law, for the cases represented in Eq. (57). Also tangent contact stress Eq. (58).

$$\begin{aligned} \mathcal{A}_{sln+1}^{i+1} &:= \left\{ j \in \mathcal{A} | \mathbf{t}_{co}^\tau \geq \mathscr{F}_{n+1}^{i+1} \right\} \\ \mathcal{A}_{stn+1}^{i+1} &:= \left\{ j \in \mathcal{A} | \mathbf{t}_{co}^\tau < \mathscr{F}_{n+1} \right\} \end{aligned} \tag{56}$$

$$\mathscr{F} = \mu \left(k\mathbf{n} \cdot \boldsymbol{\lambda} + \varepsilon_n \bar{g}_n \right) \tag{57}$$

$$\mathbf{t}_{co}^\tau = \| k\boldsymbol{\tau} \cdot \boldsymbol{\lambda} + \varepsilon_\tau \tilde{\mathbf{u}}_\tau \| \tag{58}$$

16:            Compute the corresponding residual to check Eq. (59).

$$\|\mathbf{r}_u\| < tolerance_u, \ \|\mathbf{r}_{\lambda_n}\| < tolerance_{\lambda_n}, \ \|\mathbf{r}_{\lambda_\tau^{sl}}\| < tolerance_{\lambda_\tau^{sl}}, \ \|\mathbf{r}_{\lambda_\tau^{st}}\| < tolerance_{\lambda_\tau^{st}} \tag{59}$$

17:            Converged if $\mathcal{A}_{sln+1}^{i+1} = \mathcal{A}_{sln+1}^i$, $\mathcal{A}_{stn+1}^{i+1} = \mathcal{A}_{stn+1}^i$, $\mathcal{I}_{n+1}^{i+1} = \mathcal{I}_{n+1}^i$ and residuals Eq. (59).
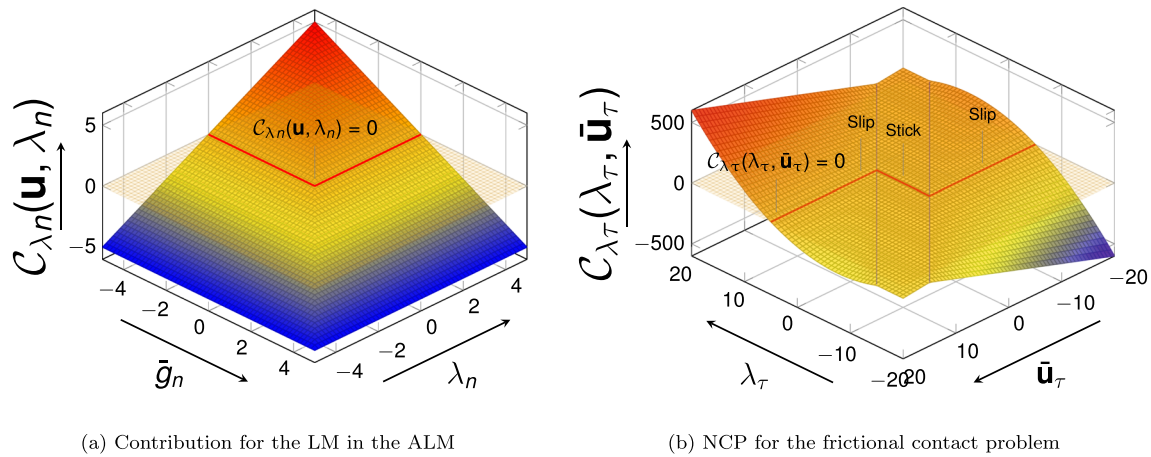

(a) Contribution for the LM in the ALM

(b) NCP for the frictional contact problem

Fig. 25 Nodal NCP function, or *Lagrangian* ($\mathcal{L}$)

Appendix 1.4: Active set strategy (Semi-smooth Newton Raphson)

As previously stated, the fully discretised *unilateral* contact problem introduces one significant complexity in the problem resolution. This issue is the contact specific inequality constraints, which introduces two different sets of discrete active and inactive constraints, which are unknown *a priori*. This previous dilemma does not appear for the mesh tying case, where the subsets are known *a priori*. From a mathematical point of view, this introduces an additional source of non-linearity apart from the already existing geometric and material non-linearity. This issue can be solved with the consideration of an appropriate strategy, a common approach is the Primal-Dual Active Set Strategies (PDASS).

The principle behind any active set strategy for *unilateral* contact is to iterate looking for the correct subset of master–slave nodes in contact until there is no variation in the respective subsets in the given time step. On the other hand, the contact non-linearity cannot be simply solved in application of the PDASS. This is because finding the correct active set $\mathcal{A}$ cannot be resolved by a standard *Newton–Raphson* type approach.

It can be affirmed that in each one of the non-converged subsets we can apply a standard *Newton–Raphson* type algorithm, in the same manner it is applied to the other types of non-linearity. These non-converged subsets are obtained from rearranging the KKT conditions. In Popp [33] the discrete KKT conditions are reformulated within a so-called Non-Linear Complementary Function (NCP), this NCP is equivalent to the *Lagrangian* ($\mathcal{L}$) contribution for the LM in the ALM, therefore in case of consider an ALM formulation it is *de facto* considered in the *Lagrangian* ($\mathcal{L}$) definition. Equation (60) shows the expression which defines the frictionless NCP. This corresponds with the augmented normal contact pressure $\bar{\boldsymbol{\lambda}}_n$ presented before Eq. (29), and the criteria will

consist on activate/inactivate the corresponding node if the augmented contact pressure $\bar{\lambda}_n$ is in compression or traction correspondingly. The graphical representation can be seen in Fig. 25a, where the equivalence with the KKT conditions is indicated in red colour, and this is drifted accordingly to the penalty ε contribution.

$$\mathcal{C}_{\lambda n} = k\lambda_n - max(0, k\lambda_n + \varepsilon\bar{g}_n) \tag{60}$$

Hence, the PDASS considered accommodates derivative information on the subsets, allowing the resolution in considering *Newton–Raphson* algorithm also for the contact non-linearity.

The reformulation of frictional contact conditions is similar to the frictionless case. As well as in the former case, the LM contribution of the *Lagrangian* ($\mathcal{L}$) in the ALM (34) replaces the NCP presented in *Popp* [33] and Gitterle [35]. This NCP takes the form of a two component vector equation and is written as (61), the visual representation can be seen in Fig. 25b This representation shows a distinctive behaviour for the slip/stick states in the similar manner to the one presented in the Fig. 8b for the frictional *Lagrangian* ($\mathcal{L}$) contribution. For the frictional problem, the PDASS is taken into consideration in considering the workflow presented in Sect. 3.

$$\mathcal{C}_\tau(\boldsymbol{\lambda}_\tau, \tilde{\mathbf{u}}_\tau) = max(\mu\tilde{\lambda}_n, \|\tilde{\boldsymbol{\lambda}}_\tau\|)\boldsymbol{\lambda}_\tau - \mu max(0, \lambda_n)\tilde{\boldsymbol{\lambda}}_\tau \tag{61}$$

References

1. Akasaka T (1981) Structural mechanics of radial tires. Rubber Chem Technol 54(3):461–492
2. Janiszewski J, Baranowski P, Malachowski J, Wekezer J (2016) Detailed tyre FE modelling with multistage validation for dynamic analysis. Mater Des 96:68–79

3. Kilic N, Erdik E, Bedir S (2010) Numerical simulation of armored vehicles subjected to undercarriage landmine blasts. Shock Waves 37:685–693

4. Micheli GB, Neves RRV, Alves M (2010) An experimental and numerical investigation on tyre impact. Int J Impact Eng 37:685–693

5. Gotowicki P, Baranowski P, Bogusz P, Malachowski J (2012) Assessment of mechanical properties of offroad vehicle tire: Coupons testing and FE model development. Acta Mech Autom 6(2):12–22

6. Meschke G, Helnwein P, Liu CH, Mang HA (1993) A new 3-D finite element model for cord-reinforced rubber composites—application to analysis of automobile tires. Finite Elem Anal Des 14(1):1–16

7. Yang LM, Shim VP, Lim CT (2000) A visco-hyperelastic approach to modeling the constitutive behaviour of rubber. Int J Impact Eng 24:545–560

8. Daniel IM, Rao S, Gdouto IM (2004) Mechanical properties and failure behaviour of cord/rubber composites. Appl Compos Mater 11:353–375

9. Haggblad B, Sundberg JA (1983) Large strain solutions of rubber components. Comput Struct 17(5–6):835–843

10. Rothert H, Domscheit A, Winkelmann T (1989) Refined methods for tire computation. Tire Sci Technol 17:291–304

11. Tabaddor F, Stafford JR (1985) Some aspects of rubber composite finite element analysis. Tire Sci Technol Comput Struct 21:327–339

12. Satyamurthy K, Chang JP, Tseng NT (1988) An efficient approach for the three-dimensional finite element analysis of tires. Tire Sci Technol 16:249–273

13. Hudobivnik B, Wriggers P, Schoder J (2018) Finite and virtual element formulations for large strain anisotropic material with inextensive fibers. In: Multiscale modeling of heterogeneous structures. Lecture Notes in Applied and Computational Mechanics, vol 86. Springer

14. Hudobivnik B, Wriggers P, Aldakheel F (2020) A virtual element formulation for general element shapes. Comput Mech 66:963–977

15. Cornejo A et al (2018) Methodology for the analysis of post-tensioned structures using a constitutive serial-parallel rule of mixtures. Compos Struct 200:480–497

16. Barbu LG et al (2019) Methodology for the analysis of post-tensioned structures using a constitutive serial-parallel rule of mixtures: large scale non-linear analysis. Compos Struct 216:315–330

17. Jimenez S et al (2020) Analysis of the mock-up of a reactor containment building: comparison with experimental results. Nuclear Eng Des 359:110454

18. Jimenez S et al (2021) Failure pressure analysis of a nuclear reactor prestressed concrete containment building. Eng Struct 236:112052

19. Mataix V (2020) Development of innovative mathematical and numerical models for the study of shells deformation during industrial forming processes employing the Finite Element Method. Universitat Polit'ecnica de Catalunya

20. Gitterle M, Popp A, Gee MW, Wall WA (2010) Finite deformation frictional mortar contact using a semi-smooth Newton method with consistent linearization. Int J Numer Methods Eng 84:543–571

21. Andrade Pires FM, Doca T, Cesar de Sa JMA (2014) A frictional mortar contact approach for the analysis of large inelastic deformation problems. Int J Numer Methods Eng 51:1697–1715

22. Rossi R, Davvand P, Oñate E (2010) An object-oriented environment for developing finite element codes for multi-disciplinary applications. Arch Comput. Methods Eng 17:253–297

23. Davvand P et al (2013) Migration of a generic multi-physics framework to HPC environments. Comput Fluids 80:301–309

24. Holscher H et al (2004) Modeling of pneumatic tires by a finite element model for the development a tire friction remote sensor. In: Center of Advanced European studies and Research

25. Kohjiya S, Ikeda Y, Kato A, Nakajima Y (2018) Rubber science: a modern approach. Springer, Singapore

26. Bellomo F, Comellas E, Oller S (2016) A generalized finite-strain damage model for quasi-incompressible hyperelasticity using hybrid formulation. Int J Numer Methods Eng 105:781–800

27. Wriggers P (2008) Nonlinear finite element methods. Springer

28. Sussman T, Bathe K-J (1987) A finite element formulation for nonlinear incompressible elastic and inelastic analysis. Comput Struct 26:357–409

29. de Souza Neto EA, Peric D, Dutko M, Owen D (1996) Design of simple low order finite elements for large strain analysis of nearly incompressible solids. Int J Solids Struct 33:3277–3296

30. Korelc J, Wriggers P (2016) Automation of finite element methods. Springer, Berlin

31. Schroder J et al (2021) A selection of benchmark problems in solid mechanics and applied mathematics. Arch Comput Methods Eng 28:713–751

32. Cornejo A (2021) A fully Lagrangian formulation for fluid-structure interaction between free surface flows and multi-fracturing solids and structures. In: Universitat Polit'ecnica de Catalunya, PhD Thesis

33. Popp A (2012) Mortar methods for computational contact mechanics and general interface problems. Dissertation. Technische Universität München. https://www.lnm.mw.tum.de/staff/alexander-popp

34. Popp A et al (2010) A dual mortar approach for 3D finite deformation contact with consistent linearization. Int J Numer Methods Eng 83(11):1428–1465. https://doi.org/10.1002/nme.2866

35. Gitterle M (2012) A dual mortar formulation for finite deformation frictional contact problems including wear and thermal coupling. Dissertation. Technische Universität München, München

36. Calavalieri FJ, Cardona A (2012) An augumented Lagrangian method to solve three dimensional nonlinear contact problems. Latin Am Appl Res 42(3):281–289

37. Cavalieri FJ, Cardona A (2013) An augmented Lagrangian technique combined with a mortar algorithm for modelling mechanical contact problems. Int J Numer Methods Eng 93(4):420–442

38. Yastrebov VA (2011) Computational contact mechanics: geometry, detection and numerical techniques. Theses. École Nationale Supérieure des Mines de Paris. https://pastel.archives-ouvertes.fr/pastel-00657305

39. Yastrebov VA (2013) Numerical methods in contact mechanics. 1st edn. ISTE. Wiley. ISBN: 1848215193, 978-1-84821-519-1. http://gen.lib.rus.ec/book/index.php?md5=13d31c503eb7652c88bbdc2070470985

40. de Carvalho Rodrigues Doca T (2014) Energy wear methods for dual-mortar contact analysis of frictional problems at finite inelastic strains. PhD thesis

41. Doca T, Pires Andrade FM, Cesar de Sa JMA (2014) A frictional mortar contact approach for the analysis of large inelastic deformation problems. Int J Solids Struct 9:1697–1715

42. Yang B, Laursen TA, Meng X (2005) Two dimensional mortar contact methods for large deformation frictional sliding. Int J Numer Methods Eng 9:1183–1225

43. Wohlmuth BI (2001) Discretization methods and iterative solvers based on domain decomposition. 1st edn., Lecture Notes in Computational Science and Engineering, vol 17. Springer, Berlin. ISBN: 354041083X, 9783540410836. http://gen.lib.rus.ec/book/index.php?md5=B3E7B367C96D74D874F54DCE9DF739A8

44. Wohlmuth BI (2002) A comparison of dual Lagrange multiplier spaces for mortar finite element discretizations. ESAIM Math Model Numer Anal 36(6):995–1012. https://doi.org/10.1051/m2an:2003002

45. Pietrzak G, Curnier A (1999) Large deformation frictional contact mechanics: continuum formulation and augmented Lagrangean treatment. Comput Methods Appl Mech Eng 177:351–381

46. Cavalieri FJ, Cardona A (2015) Numerical solution of frictional contact problems based on a mortar algorithm with an augmented Lagrangian technique. Multibody Syst Dyn 35(4):353–375. https://doi.org/10.1007/s11044-015-9449-8

47. Fischer KA, Wriggers P (2006) Mortar based frictional contact formulation for higher order interpolations using the moving friction cone. Comput Methods Appl Mech Eng 195(37–40):5020–5036

48. Dias APC, Serpa AL, Bittencourt ML (2015) High-order mortar-based element applied to nonlinear analysis of structural contact mechanics. Comput Methods Appl Mech Eng 294:19–55

49. Grosch KA (1962) The relation between the friction and viscoelastic properties of rubber. In: The natural rubber producers' research association

50. Ziefle M, Nackenhorst U (2008) Numerical techniques for rolling rubber wheels: treatment of inelastic material properties and frictional contact. Comput Mech 42:337–356

51. Temizer I, Wriggers P, Hughes T (2012) Three-dimensional mortar-based frictional contact treatment in isogeometric analysis with NURBS. Comput Methods Appl Mech Eng 209:115–128

52. Rossi R, Zorrilla R, Codina R (2021) A stabilised displacement—volumetric strain formulation for nearly incompressible and anisotropic materials. Comput Methods Appl Mech Eng 377:113701

53. Reinelt J, Wriggers P (2020) Multi-scale approach for frictional contact of elastomers on rough rigid surfaces. Springer, Berlin

54. Wriggers P, Reinelt J (2009) Multi-scale approach for frictional contact of elastomers on rough rigid surfaces. Comput Methods Appl Mech Eng 198:1996–2008

55. Wagner P et al (2015) Multiscale FEM approach for hysteresis friction of rubber on rough surfaces. Comput Methods Appl Mech Eng 296(2015):150–168

56. Robert L (1991) Taylor and panagiotis panagiotopoulos. In: On a patch test for contact problems in two dimensions